ISSN : 2830-8085
DOI : https://doi.org/10.58452/jpcr.v4i1

Journal of Physical & Chemical Research

Volume 4, Issue 1, June (2025) 1-64

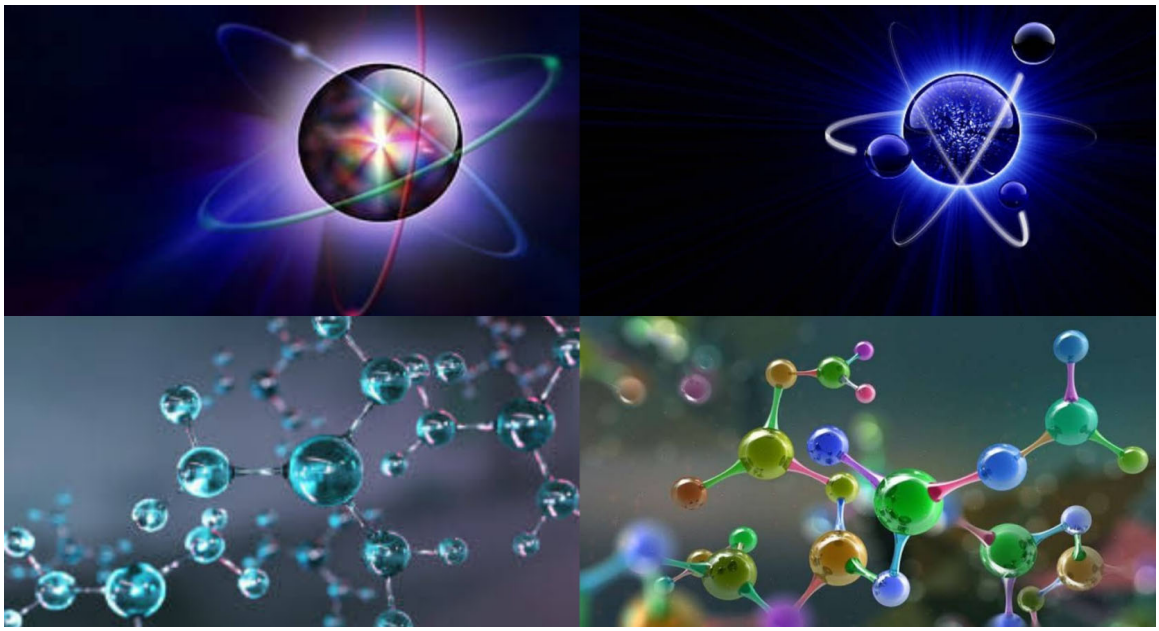

Pr. Kahoul Abdelhalim
Editor-in-Chief

First Legal Deposit: June, 2025

Journal homepage: https://ojs.univ-bba.dz

Journal of Physical and Chemical Research

- **Scientific committee**

- Laraoui Abdelghani
  alaraoui2@unl.edu
  Department of Mechanical & Materials Engineering, University of Nebraska – Lincoln, USA.
- Nuray Kup Aylikci
  nuray.aylikci@iste.edu.tr
  Department of Energy Systems Engineering, Faculty of Engineering and Natural Sciences.
  Iskenderun Technical University, Iskenderun, Hatay, Turkey.
- Volkan Aylikci
  volkan.aylikci@iste.edu.tr
  Department of Metallurgical and Materials Engineering,
  Faculty of Engineering and Natural Sciences, Iskenderun Technical University,
  Iskenderun, Hatay, Turkey.
- Latrache Abdelhakim
  abdelhakim.latreche@univ-bba.dz
  Mohamed El Bachir El Ibrahimi University, Bordj-Bou-Arreridj, Algeria.
- Abdelhalim Bencheikh
  abdelhalim.bencheikh@univ-bba.dz
  Mohamed El Bachir El Ibrahimi University, Bordj-Bou-Arreridj, Algeria.
- Bentabet Abdelouahab
  abdelouahab.bentabet@univ-bba.dz
  Mohamed El Bachir El Ibrahimi University, Bordj-Bou-Arreridj, Algeria
- Lebgaa Nodjoud
  noudjoud.lebga@univ-bba.dz
  Mohamed El Bachir El Ibrahimi University, Bordj-Bou-Arreridj, Algeria.
- Bahloul Ahmed
  ahmed.bahloul@univ-bba.dz
  Mohamed El Bachir El Ibrahimi University, Bordj-Bou-Arreridj, Algeria.
- Hellati Abdelhak
  abdelhak.hellati@univ-bba.dz
  Mohamed El Bachir El Ibrahimi University, Bordj-Bou-Arreridj, Algeria.
- Boufassa Samia
  samia.boufassa@univ-bba.dz
  Mohamed El Bachir El Ibrahimi University, Bordj-Bou-Arreridj, Algeria.
- Benamrani Ammar
  ammar.benamrani@univ-bba.dz
  Mohamed El Bachir El Ibrahimi University, Bordj-Bou-Arreridj, Algeria.
- Daoud Salah
  salah.daoud@univ-bba.dz
  Mohamed El Bachir El Ibrahimi University, Bordj-Bou-Arreridj, Algeria.
- Riad Ayache
  riad.ayache@univ-bba.dz
  Mohamed El Bachir El Ibrahimi University, Bordj-Bou-Arreridj, Algeria.
- Khelladi Mohamed Ridha
  mohamedridha.khelladi@univ-bba.dz ; redha2022@yahoo.fr
  Mohamed El Bachir El Ibrahimi University, Bordj-Bou-Arreridj, Algeria.
- Tabti Salima
  salima.tabti@univ-bba.dz ; thabti_sa@yahoo.fr
  Mohamed El Bachir El Ibrahimi University, Bordj-Bou-Arreridj, Algeria.
- Chikouche Imene
  imene.chikouche@univ-bba.dz ; chikouche_imene@yahoo.fr
  Mohamed El Bachir El Ibrahimi University, Bordj-Bou-Arreridj, Algeria.
- Khalfallah Farid
  f.khalfallah@univ-bba.dz ; khal.far@gmail.com

Mohamed El Bachir El Ibrahimi University, Bordj-Bou-Arreridj, Algeria.

- Daoudi Salim
  s.daoudi@univ-bba.dz ; salzdg@gmail.com
  Mohamed El Bachir El Ibrahimi University, Bordj-Bou-Arreridj, Algeria.
- Sahnoune Yassine
  yassine.sahnoune@univ-bba.dz ; sahnoun.y34@gmail.com
  Mohamed El Bachir El Ibrahimi University, Bordj-Bou-Arreridj, Algeria.
- Bioud Nadhira
  nadhira.bioud@univ-bba.dz
  Mohamed El Bachir El Ibrahimi University, Bordj-Bou-Arreridj, Algeria
- Kasri Yazid
  yazidkasri@yahoo.fr
  University of Béjaia.
- Deghfel Bahri
  badeghfel@gmail.com
  University of M'sila
- Baadji Nadjib
  nadjibbaadji@gmail.com
  University of M'sila
- Lamiri Leila
  l.lamiri@crti.dz
  Unité de Développement des Couches, Minces et Applications (UDCMA-CRTI), Sétif.
- Laidoudi Samiha
  samiha.laidoudi@univ-bba.dz
  Departement of Electronics; Faculty of Sciences and Technology, University Mohamed El Bachir El Ibrahimi of Bordj Bou Arreridj 34030, Algeria..
- Belgherbi Ouafia
  o.belgherbi@crti.dz
  Unité de Développement des Couches, Minces et Applications (UDCMA-CRTI), Sétif.
- Kaabi Ilhem
  Kaabi.ilhem@univ-setif.dz
  Ferhat Abbas University -Sétif 1-, Algeria.
- Boudour Samah
  s.boudour@crti.dz
  Unité de Développement des Couches Minces et Applications (UDCMA-CRTI)
- Belhadj Hamza
  email: hbelhadj@cdta.dz , belhadjhamza@gmail.com
  Unité de Recherche en Nanosciences et Nanotechnologies
  Centre de Développement des Technologies Avancées (CDTA)
- Hamza Djamel
  Email : djamel.hamza@univ-setif.dz
  Département de chimie, Faculté des Sciences, Université Ferhat ABBAS- Sétif 1
- Hayette Faid
  hayettefaid@univ-bba.dz
  Mohamed El Bachir El Ibrahimi University, Bordj-Bou-Arreridj, Algeria.
- Fares Nor El Houda
  norelhouda.fares@univ-bba.dz; fares_houda@yahoo.fr
  Département Recherche Opérationnelle, Faculté Mathématiques et Informatiques
  Mohamed El Bachir El Ibrahimi University, Bordj-Bou-Arreridj, Algeria
- Hamla Mariem
  Email : meriem.hamla@univ-bba.dz
  Mohamed El Bachir El Ibrahimi University, Bordj-Bou-Arreridj, Algeria.
- Amamra Samra
  Email : samra.amamra@univ-bba.dz
  Mohamed El Bachir El Ibrahimi University, Bordj-Bou-Arreridj, Algeria.

Journal of Physical and Chemical Research
Volume 4, Issue 1, June (2025) 1-64

Physical Research

Chemical Research

Journal of Physical & Chemical Research

Journal homepage: https://ojs.univ-bba.dz

The effect of In, Cu Co-doping on the electronic structure and optical properties of ZnS: First principal calculations

H. Hedjar[1,2*], A. Boukortt1, I. Bouzateur2, S. Meskine[1], A.H. Tabti[2], S. Derkaoui[2]

[1]Elaboration and Characterization Physico-Mechanical and Metallurgical of Materials Laboratory (ECP3M), Abdelhamid Ibn Badis University-Mostaganem. Route nationale N°11, Kharrouba, 27000, Mostaganem Algeria.
[2] University of Tissemsilt, faculty of Science and Technology, 38000, Algeria
** Corresponding author: Tel./Fax:+213-697-060-006; E-mail address: h.hedjar@univ-tissemsilt.dz.*

Article history
Received March 8, 2025
Accepted for publication April 27, 2025

Abstract

The effects of In and Cu co-doping ZnS on the structural, electronic and optical properties are investigated by using the full-potential linearized augmented plane wave method (FP-LAPW) with generalized gradient approximation plus Becke–Johnson potential as exchange-correlation potential, in a cubic structure. The calculated lattice parameter of Un-doped ZnS was in a good argument with the other theoretical calculations, and it was found to be increased by In, Cu co-doping. The electronic band structures are calculated and represented. The un-doped ZnS shows a semiconductor character with a direct band gap. Hence, it saves the semiconductor character with a direct band gap with some change in its value. It decreases by co-doping with In and Cu. Moreover, the real and imaginary part of the dielectric function as and the absorption coefficient attains its maximum in the near UV-Visible region. This theoretical study intensifies the understanding of the novel performances of In, Cu co-doped ZnS for optoelectronic applications.

Keywords: ZnS; doped, co-doped, FP-LAPW, GGA+mBJ

1. Introduction

Due to its potential applications in science and industry, semiconductor nanomaterials have received an immense amount of attention from researchers in recent years. Because of its chemical and physical characteristics, the II-VI group of semiconductors is widely used in a wide range of applications [1-2]. Zinc sulfide (ZnS) is widely recognized as a highly versatile and technologically significant II-VI compound smiconductor. Its large exciton binding energy (40 meV), abundance in nature, and lack of toxicity make it suitable for short-wavelength optoelectronic applications. As a result, it is frequently doped with a variety of dopants [3–7]. The potential use of zinc sulfide (ZnS) in many optoelectronic applications, such as photovoltaic cells, light-emitting diodes, and sensors, has drawn a lot of attention [8-15]. To create new materials for new applications in electronic, spintronics and optoelectronics, doping and co-doping with deferent ions is a useful technique for achieving tunable electronic, magnetic and optical properties. Zinc Sulfur (ZnS) is seen as a potentially useful host semi-conductor for a massive game of ions. ZnS was doped with various ions such as: Manganese (Mn) [16], Vanadium (V) [17] Nickel [18], cobalt [19], Iron (Fe) [20] and others [21-24] and co-doping with deferent ions [25-28]

In this present work, the first time we investigated structural and optoelectronic properties of undoped and In, Cu co-doped ZnS semiconductor using the full potential linear augmented plane wave FP-LAPW [29] method within the density functional theory (DFT)[30]. The electronic exchange-correlation energy is described by generalized gradient approximation. To our knowledge, no comprehensive literature has been provided regarding the structural and optoelectronic properties of In, Cu co-doped ZnS compounds

2. Method

As part of the density functional theory (DFT) [30], implemented in the Wien2k package [31], the full-potential linearized augmented plane wave (FP-LAPW) approach [29] is used for the current computations. The exchange and correlation effects are treated by the Perdew– Burke–Ernzerhof generalized gradient approximation (GGA) [31]. The GGA +mBJ [32], is applied to optimize the corresponding potential for calculating the electronic and optical properties.

We take a supercell of 8 atoms (Fig. 1b) The RMT (muffin-tin radii) are taken to be 2.54, 2.35, 2.56 and 1.8 atomic unit (a.u.) for Zn, Cu, In and S, respectively, where RMT is the minimum radius of the muffin-tin. The self-consistent calculations are considered to be converged when the total energy of the system is stable within 10^{-5}Ryd. The integrals over the

Brillouin zone (BZ) are performed up to **136 k-points** (grid of **10 *10 *10)** meshes

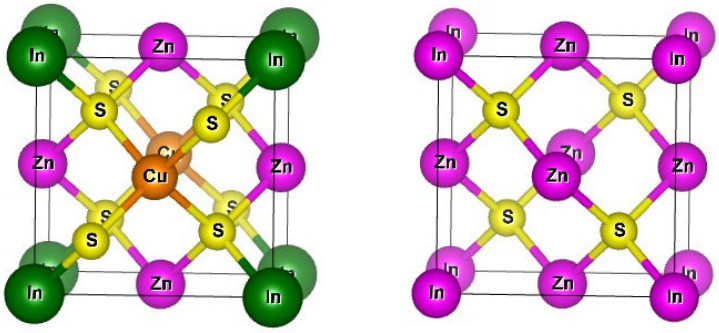

Fig.1. The crystalline structure of Un-doped ZnS and (In, Cu) co-doped ZnS.

3. Results and discussion

3.1. Structural properties

The lattice parameters are obtained by the calculation of the total energy as a function of the volume using Murnaghan's equation of states (EOS) [55]. The structural parameters are classified in Table1 In the case of un-doped ZnS, the lattice parameter is 5.44 Å. It is found to be very close with other calculations [2, 42]. However, the lattice parameter of ZnS is Increased by co-doping with In and Cu. This change in the values of the lattice parameters is due to the dimension of ionic radius of the Cu^{2+} (0.73Å) [1] and In^{2+} (0.80Å) [34] which are larger comparing to the ionic radius Zn^{2+}(0.74 Å) [26].

Table 1. The calculated equilibrium constant a (A°), bulk modulus B (GPa), first order pressure derivative of the bulk modulus B0 with others experimental and theoretical works

Compound		a(Ang)	B(GPa)	B'
Un-doped ZnS	Our work	5.45	76.04	4.95
	Other works	5.42[12]	89.22[12]	5.1[12]
(In, Cu) co-doped ZnS	Our work	5.56	66.25	4.95
	Other works	-	-	-

3.2.Electronic properties

Moreover, to understand the effect of In, Cu co-doping on the electronic properties of ZnS, the electronic band structures of Un-doped ZnS and (In, Cu) co-doped ZnS are calculated by the GGA and GGA+mBJ approximations.

These calculations indicate that the un-doped ZnS present a direct bandgap at $(\Gamma - \Gamma)$ point of the Brillouin zone it is seen that the minimum of the conduction band (CB) is situated at (Γ) point of the Brillouin zone and the maximum of the valence band (VB) is situated at (Γ) point. In the case of (In, Cu) co-doped ZnS. it is seen that the minimum of the conduction band (CB) is situated at (Σ) point of the Brillouin zone and the maximum of the valence band (VB) is situated at (Σ) point and this means that this system has also a direct bandgap at (Σ -Σ) point of the Brillouin zone. While, we noted a large decrease in its value from 1.51eV to 0.654 eV by GGA and from 3.56 eV to 0.654 eV by GGA . The change in the value and the nature of band gap energy is mainly due to the *sp–d* exchange interactions between the band electrons and the localized *d* electrons of the Cu, In ions [12].

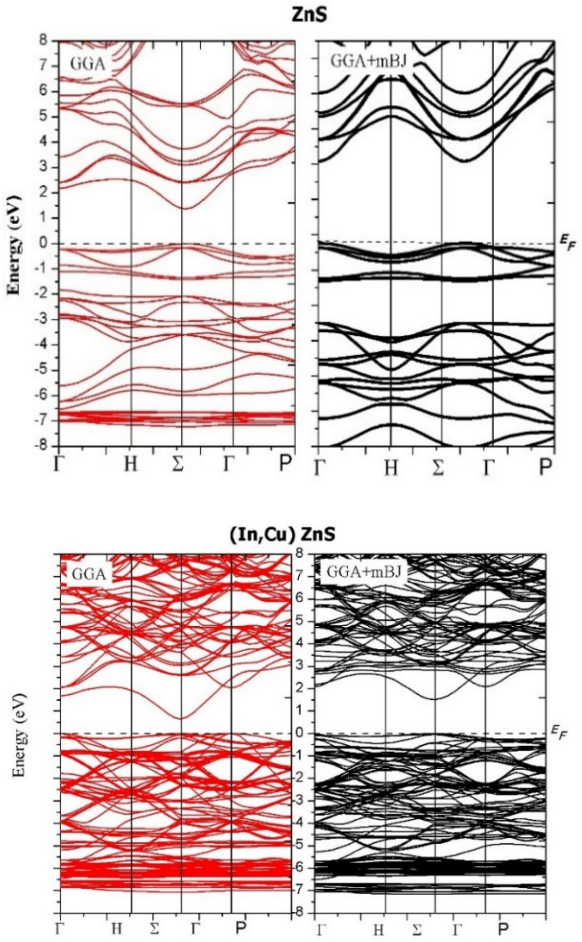

Fig.2. The band structures of Un-doped ZnS and (In, Cu) co-doped ZnS by GGA and GGA+mBJ approximation.

Table 2. The energy band gap of Un-doped ZnS and (In, Cu) co-doped ZnS by GGA and GGA+mBJ in comparison with others experimental ant theoretical works

Compound		E_g(eV)	
		GGA	GGA+mBJ
Un-doped ZnS	Our work	1.51	3.56
	Other works	[12]	[12]
(In, Cu) co-doped ZnS	Our work	0.654	
	Other works	-	-

3.3.Optical properties

The study of the optical properties of condensed matter has proven to be a important tool to understand the electronic properties of material. All the calculated optical parameters are getting from the dielectric function$\varepsilon(\omega)$. It is given by [35]:

$$\varepsilon(\omega) = \varepsilon_1(\omega) + i\varepsilon_2(\omega)$$

ε_1 and $\varepsilon_2$are the real and imaginary part of the dielectric function and is the angular frequency. The real and imaginary parts of the dielectric function and the absorption coefficient as a function of the energy of Un-doped ZnS and (In, Cu) co-doped ZnS by GGA and GGA+mBJ approximation are plotted in **Fig.4 to Fig.6**.

Fig.4. presents the real part of the dielectric function. We can extract from the ε_1 curves the calculated static dielectric coefficient $\varepsilon_1(0)$. For un-doped ZnS, it is 3.5 and 3.65 by GGA and GGA+mBJ approximation. For (In, Cu) co-doped ZnS, we noted that $\varepsilon_1(0)$ increase in comparison to the un-doped ZnS and it is 4.70 and 6.5 by GGA and GGA+mBJ approximation , respectively

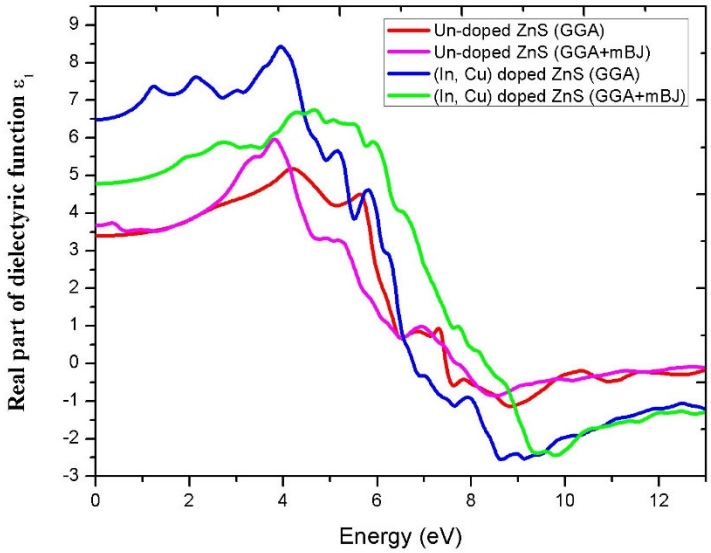

Fig.4. The real parts of dielectric function ε_1 as function of energy of Un-doped ZnS and (In, Cu) co-doped ZnS by GGA and GGA+mBJ approximation.

The imaginary part of dielectric function ε_2 as function of energy of Un-doped ZnS and (In, Cu) co-doped ZnS by GGA and GGA+mBJ approximation are presented in **Fig.6.** The most important value in these curves is the first transition which is considered by the band gap. The corresponding values of un-doped ZnS are 1.98 eV and 3 .00 eV by GGA and GGA+mBJ and 0.65 eV and 1.5 eV for (In, Cu) co-doped ZnS by GGA and GGA+mBJ approximation.We can see that all systems have a semiconducting character

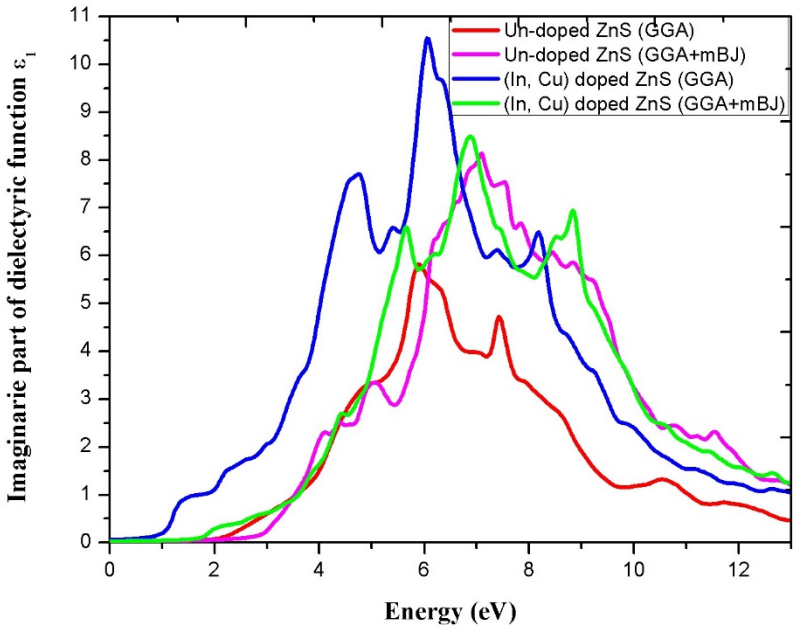

Fig.5. The imaginary parts of dielectric function $\varepsilon_1$as function of energy of Un-doped ZnS and (In, Cu) co-doped ZnS by GGA and GGA+mBJ approximation.

In Fig.6, we plotted the absorption coefficient as function of wave length for both systems by GGA and GGA+mBJ. the absorption coefficient is related to the imaginary part of dielectric function by:

$$\alpha(\omega) = \frac{1}{n(\omega)}\varepsilon_2(\omega)$$

We had noted that the two systems Un-doped ZnS and (In, Cu) co-doped have strong absorption in the range from 6 eV to 10 eV, corresponding to the UV region. Hence, the intensity of the absorption coefficient is decreased by co-doping with In and Cu ions.

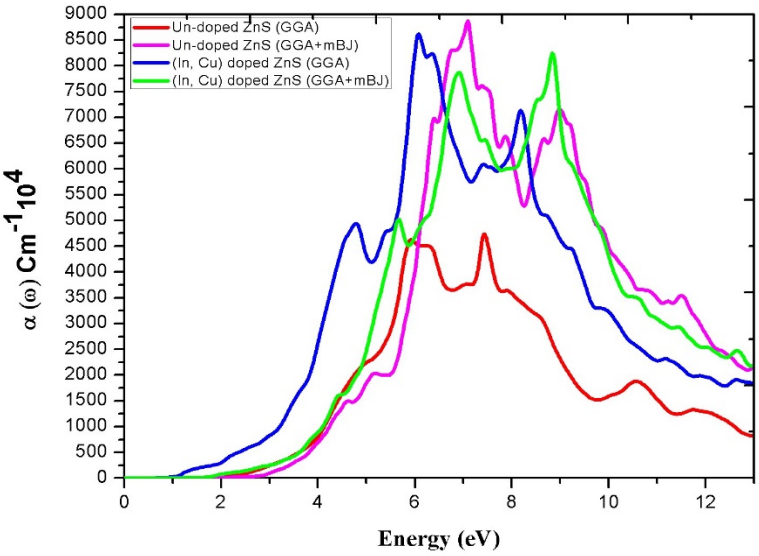

Fig.6. The absorption coefficient $\alpha(\omega)$as function of energy of Un-doped ZnS and (In, Cu) co-doped ZnS by GGA and GGA+mBJ approximation

4. Conclusion

In this study, we have investigated the effects of In and Cu co-doping ZnS on the structural, electronic and optical properties are investigated by using the full-potential linearized augmented plane wave method (FP-LAPW) with generalized gradient approximation plus Becke–Johnson potential as exchange-correlation potential, in a cubic structure. The calculated lattice parameter of Un-doped ZnS was in a good argument with the other theoretical calculation, and it was found to be increased by In, Cu co-doping. The electronic band structures are calculated and represented. The un-doped ZnS shows a semiconductor character with a direct band gap. Hence, it saves the semiconductor character with a direct band gap with some change in its value. It decreases by co-doping with In and Cu. Moreover, the real and imaginary part of the dielectric function as and the absorption coefficient attains its maximum in the near UV-Visible region. This theoretical study intensifies the understanding of the novel performances of In, Cu co-doped ZnS.

References

[1] Sathishkumar M, Saroja M, Venkatachalam M , Optik (2019)
[2] Geoffrey Tse, Computational Condensed Matter. 28 (2021), e00572.
[3] M. Sheraz Khan, Lijie Shi, Bingsuo Zou, Sajjad Ali, Comput. Mater. Sci. 174 (2020), 109491.
[4] Jing Liu, Shuaipeng Yue, Chem. Phys. Lett. 801 (2022), 139716.

[5] B. Poornaprakash, P.T. Poojitha, U. Chalapathi, S. Ramu, R.P. Vijayalakshmi, SiHyun Park, Ceram. Int. 42 (2016) 8092–8097.
[6] Akeem AdekunleAdewale, Chik Abdullah, Tijjani Adam, Joshua Tolulope Majekodunmi, Mondiu OlayinkaDurowoju, Mater. Today Commun. 27 (2021), 102077.
[7] D.E. Aimouch, S. Meskine, R. Hayn, A. Boukortt, Phys. E Low-dimens. Syst. Nanostruct. 84 (2016) 401.
[8] Muhammad SherazKhan, LijieShi, Bingsuo Zou, HamidUllah. Optik. 204 (2020), 164162
[9] Y. Lei, F.F. Chen, A facile solvothermal method to produce graphene-ZnS composites for superior photoelectric applications. Appl. Surf. Sci. 308 (2014) 206–210.
[10] S. Fathhoor Rabbani, I.B. Shameem Banu, J. Alloys Compd. 695 (25) (2017) 3131–3138.
[11] AhmedAL-Osta, Adnan Alnehia, A.A. Qaid, Hassan T. Al-Ahsab, AnnasAl-Sharabi. Optik. 214 (2020), 164-831.
[12] H. Hedjar, S. Meskine, A. Boukortt, H. Bennacer, M.R. Benzidane, Computational Condensed Matter 30 (2022), e00632.
[13] Y. Liao, F. Yu, L. Long, B. Wei, Low-cost and reliable thin film encapsulation for organic light emitting diodes using magnesium fluoride and zinc sulfide Thin Solid Films 519 (2011) 2344–2348
[14] B. Poornaprakash, U. Chalapathi, M. Reddeppa, S.-H. Park, Superlattice. Microst. 93 (2016) 104–109.
[15] S.K. Mani, S. Manickam, V. Muthusamy, Antimicrobial Activity and Photocatalytic Degradation Properties of Zinc Sulfide Nanoparticles Synthesized by Using Plant Extracts. J. Nanostruct. 8(2) (2018) 107-118.
[16] X. Ma, J. Song, Z. Yu, The light emission properties of ZnS:Mn nanoparticles. Thin Solid Films. 519 (2011) 5043–5050
[17] Q. Mahmood, G. Murtaza, R. Ahmad, T. Hussain, I.G. Will. Current Applied Physics. 16 (2016) 361-370.
[18] Sanjeev Kumar , C. L. Chen, C. L. Dong, Y. K. Ho, J.F.Lee , T. S. Chan, R.Thangave, T. K. Chen, B. H. Mok, S. M.Rao, M. K. Wu. Journal of Alloys and Compounds. 554(2013)357-362.
[19] Q. Mahmood, S.M. Alay-e-Abbes, M. Hassan, N. A. Noor. Journal of Alloys and Compounds. 688(2016)899-907
[20] B. Poornaprakash, U. Chalapathi, S.V. Prabhakar . Appl. Phys. A 123 (2017) 275-285.
[21] M. Elisa, I.C. Vasiliu, I.D. Feraru . J. Sol-Gel. Sci. Technol. 73 (2015) 660-665.
[22] H.Absike, H. Labrim, B. Hartiti, K.Douhou, H.Ez-Zahraouy. Journal of Physics and Chemistry of Solids.132(2019)10-17.
[23] Hina Naz, Rai Nauman Ali, Xingqun Zhu, Bin Xiang. Physica E: Low-dimensional Systems and Nanostructuraes. 100(2018)1-6.
[24] Hongxia Chen. Magnetism and Magnetic Materials. 324 (2012) 2086–2090.

[25]Hedjar, H,Meskine, S.,Boukortt, A.,Bennacer, H.Benaouad, A. Computational Condensed Matter; 33(2022)e00746.
[26]B. Poornaprakash, P.T.Poojitha, U.Chalapathi, K.Subramanyam, Si-HyunPark. J. Physica E. 83 (2016) 180-185.

[27] B. Poornaprakash, U. Chalapathi, Mirgender Kumar, S.V. Prabhakar Vattikuti, Beerelli Rajitha, P.T. Poojitha, Si-Hyun Park, Mater. Sci. Semicond. Process. 121 (2021), 105395
[28] B. Poornaprakash, P.T. Poojitha, U. Chalapathi, K. Subramanyam, Si-HyunPark, Phys. E Low-dimens. Syst. Nanostruct. 83 (2016) 180–185.
[29] P. Blaha, K. Schwarz, G.K.H. Madsen, D. Hvasnicka, J. Luitz, Vienna University of Technology (2001). Austria**.**
[30] P. Hohenberg, W. Kohn, Phys. Rev. B 864 (1964) 136.
[31] K. Schwarz, P. Blaha, Comput. Mater. Sci. 28 (2003) 259
[32] J.P. Perdew, K. Burke, M. Ernzerhof, Phys. Rev. Lett. 77 (1996) 3865.
[33]Evren G. Özdemir, Fadime I. BalmumcuPhysica B: Condensed Matter 674 (2024) 415544
[34]R. Banyal , A. sudhaik, R. kumar , Sonu , P . Raizada , T.Ahamad , S. Kaya , M. M. Maslov , V.Chaudhary , C. Mustansar Hussain , P. Singh Journal of Physics and Chemistry of Solids (2024), 112132
[35]. M. Fox, Optical Properties of Solids (Oxford Univ. Press, Oxford, 2011).

J. Phys. &Chem. Res. 4, Issue 1, June (2025) 10–20

Journal of Physical & Chemical Research

Journal homepage: https://ojs.univ-bba.dz

A valorization of agricultural waste for the preparation of an environmentally sustainable material

Sahi Samira[1*], Khalfi Islam[2], Assili Walid[2]

[1]Laboratoire des Matériaux Polymères Avancés, Faculté de Technologie, Université A. MIRA de Bejaia, Bejaia, 06000, Algérie.
[2] Ecole Nationale Polytechnique d'Alger, 016000, Algérie.

** Corresponding author: E-mail address: samira.sahi@univ-bejaia.dz.*

Article history
Received March 8, 2025
Accepted for publication April 24, 2025

Abstract

The valorization of agricultural waste is a critical area of research aimed at transforming what is often considered waste into valuable eco-friendly materials. This study has two objectives: firstly, to design a composite material based on a thermoplastic matrix (PVC) reinforced with vegetable fibres, which is chemically treated with acetic anhydride to improve the fibre-matrix interface. Secondly, to study the effect of this treatment on the physico-mechanical properties of resulting materials. The composites developed have been characterized by various analysis techniques, namely: tensile, hardness, water uptake and density tests. The recorded results show that increasing the load rate of the chemically treated fibre tends to decrease the elongation and breaking stress of the composites and increase their hardness and stiffness.

Keywords: Polymeric materials, Polyvinyl chloride, natural fiber, Acetic anhydride.

1. Introduction

For almost a century, the study and design of composite materials have attracted great interest in the many and varied fields of modern chemistry. Natural fiber composites occupy an important place in the history of technology. The development of plant resources provides a highly attractive alternative to environmental, ecological, social and economic problems, the growing problem of waste, environmental legislative standards and the depletion of fossil resources [1]. The search for sustainable green technologies has led scientific research to focus on the development of green composite materials based on cellulosic plant fibers. This new category of materials is characterized by properties such as high rigidity, low cost, low density and environmental friendliness, since they are derived from renewable and biodegradable resources. It also requires little energy to produce, and offers good thermal and acoustic insulation [2]. However, the lack of adhesion with polymer matrices is a difficulty that may prevent the widespread use of plant fibers in composites. The hydrophobic nature of most synthetic polymers and the hydrophilic nature of cellulosic fibers adversely affect interfacial adhesion [3]. To overcome this problem, it is generally necessary to modify the surface of the fibers to improve their adhesion to the polymer matrix. It has been shown that appropriate treatment of cellulosic fibers can result in compatibility with the polymer matrix, improving composite quality and reducing moisture absorption [4].
Chemical modification of the fiber surface enables coupling between highly hydrophilic cellulose fibers and hydrophobic polymers. There are various chemical treatments for natural fibres: alkaline treatment, acetylation, benzylation, treatment with silane, etc [5].
Among natural fibers, date karnel flour fibers are attracting increasing attention from researchers. However, the majority of research work has focused on adding value to these pits in the form of activated charcoal, as a supplement in livestock feed, in traditional medicine and for its antimicrobial and antiviral properties, and in the preparation of citric acid and proteins [6].

2. Method

2.1 Materials

Date kernel flour (DKF) with a particle size ≤ 300 µm, density of 0.72 and a relative humidity of 12% [7]. The date kernel used come from different varieties of Algerian dates. Polyvinyl chloride (PVC) used is the SE1200 type, supplied by CABEL ‘Câblerie électrique’ of Algiers, Algeria. This polymer has the following physical properties: K-Wert, from 70.2 to 72.0 with a density of 0.521.

2.2.1 Pre-treatment of date kernel flour

Date kernel flour was pre-treated several times, as mentioned in our previous study [7]:
- Several washes with ordinary water to remove as many impurities as possible, followed by a wash with distilled water,
- Drying in the open air for 48 hours,
- Drying in an oven at 60°C for 24 hours,
- Grinding with an electric grinder to obtain a finer grain size,
- Sieving with a series of sieves to obtain a particle size of 100 µm.

2.2.3 Acetylation of DKF

DKF was dissolved in distilled water at room temperature. The pH was adjusted with 1 M NaOH to 8.0-8.5. 8 g of acetic anhydride was added to the blend and then mechanically stirred for 30 min. The blend was washed with distilled water three times and dried at 35 °C.

2.2.4 Samples preparation

The different materials with varying fiber content from 0 to 30% (table 1), were prepared using calendering and compression molding working with 170°C of temperature and with pressure of 300 kN. Plates of 250×250×2 mm^3 are obtained, which will be used for cutting samples in the form of dumbbells.

Table 1. Weight compositions of the various PVC/DKF and PVC/TDKF formulations.

Formulations / Compositions (%)	F10	F20	F30
DKF	10	20	30
TDKF	10	20	30
PVC	90	80	70

2.2.5 Density test

The density of the samples was determined by measuring the Archimedes' buoyancy exerted on the volume of sample immersed in distilled water at a known temperature. It was determined using a Model DSM Density Meter**.**

2.2.6 Water absorption test

The water absorption test is carried out according to ASTM D7031-04. The samples immersed in distilled water at room temperature with stirring. The samples are weighed every 24 hours until their mass is stabilized. The

variation of mass is given by the following formula:

$$\Delta m\ (\%) = \frac{m-mo}{m}.100 \quad (1)$$

Δm : the water absorption (%),
m : the final mass of the sample
m_0 : the initial weight of the sample

2.2.7 Hardness test

Measurement of shore D hardness in accordance with standard NF T51-109 using a Shore D durometer was carried out at CABEL 'Câblerie Electrique' in Algiers, Algeria. The test consisted of subjecting the pointed steel needle of a shore D durometer to a force tending to push it onto 5×5 cm² plates with a mass of 5g. The durometer measures between 100 and 0 (100 maximum hardness, zero penetration, 0 maximum penetration). Penetration is indicated by a direct reading on the durometer after 15 seconds.

2.2.8 Tensile test

The mechanical behaviour of the composites elaborated was determined using an MTS Criterion tensile testing machine, in accordance with standard NFC 32-200 using computer-controlled TXW-type software. The tests were carried out at a pulling speed of 50 mm.min-1. The machine gives the force F as a function of elongation ($L-L_0$), where L_0 is the initial length of the specimen. The machine is connected to a computer, which performs all the necessary calculations and plots the stress-strain curves using software such as Test X pertV10.11. Five specimens were tested for each formulation. These tests were used to determine Young's modulus, strain and stress.

3. Results and discussion

3.1 Density test

Figure 1 shows that the incorporation of DKF in the PVC leads has not affect the density materials compared to PVC. This result is explained by the low density of the DKF. Comparing the results of the density test on the PVC/DKF composites elaborated with those on the PVC/TDKF composites prepared for the same loading rates, it can be seen that the incorporation of DKF into the PVC has no effect for loading rates of 10% and 20%. At a filler content of 30%, the density is lower than that of untreated composites.

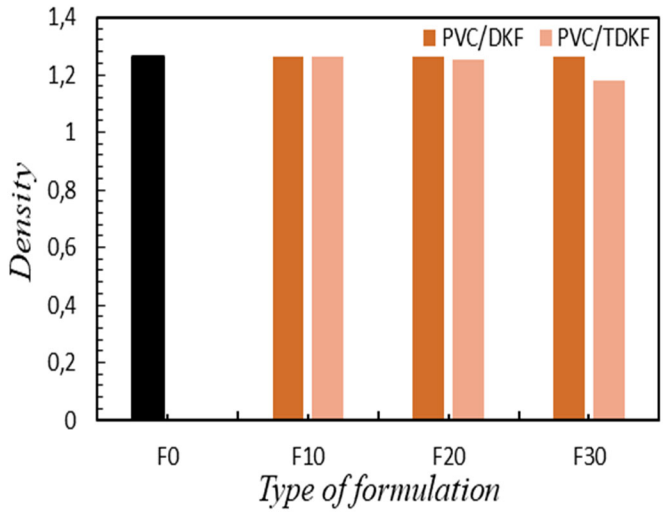

Figure 1. Density of PVC and (PVC/DKF and PVC/TDKF) composites for different formulations.

3.2 Water absorption test

The water uptake of pure PVC and PVC/DKF and PVC/TDKF composites are shown in Fig. 2. Moisture uptake increased with immersion time and rapid moisture uptake was observed for all samples within the first few days of immersion, but this decreased slowly with time. The decrease in the rate of moisture uptake with time of immersion could be due to the higher absorption of water molecules by fibre. When all of the available hydroxyl groups are used up in this way, the water absorbed became less. It was found that the water absorption of LDPE/TDKF composites is less than for those prepared with DKF. This is due to the fact that DKF is more hydrophilic that TDKF [7]. For the pure PVC, there was a very low water absorption which is of the order of 0.038 %, which is due to the hydrophobic nature of this polymer.

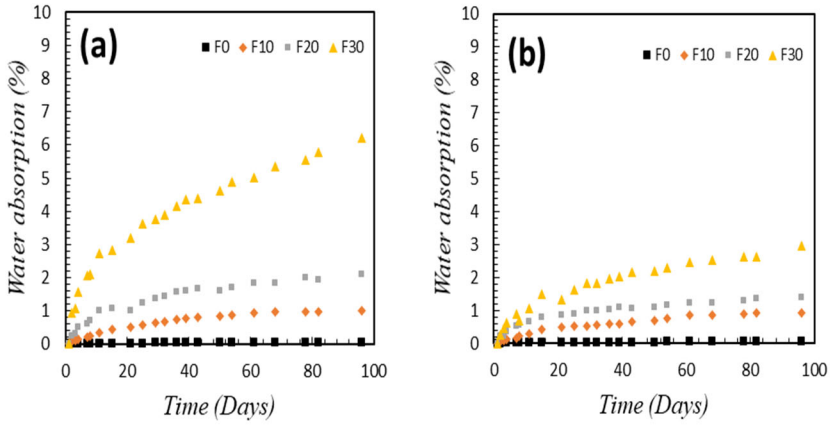

Figure 2. Water absorption of PVC, (a): PVC/DKF and (b): PVC/TDKF composites

3.3 Hardness test

The evolution of the hardness of PVC/DKF composites as a function of the filler content is shown in Fig. 3. It can be seen that the hardness increases with increasing filler content in the matrix. These results are to be expected, since date stone flour has a hardness that increases the hardness of PVC/DKF composites. An increase of 4.61%, 6.15% and 7.69% is recorded for composites filled with 10, 20 and 30% TDKF respectively, compared with virgin PVC.

Comparing the Shore hardness results of the PVC/DKF and PVC/TDKF composites, it can be seen that the composites filled with TDKF show a higher hardness than those filled with FNDB. For a loading ratio of 20%, the hardness increased from 66 to 69 for the PVC/DKF and PVC/TDKF composites respectively. This increase is explained by the good dispersion of the fiber in the matrix with a reduction in voids and stronger fiber-matrix interfacial adhesion [5]. These results are in agreement with other research work [8-10].

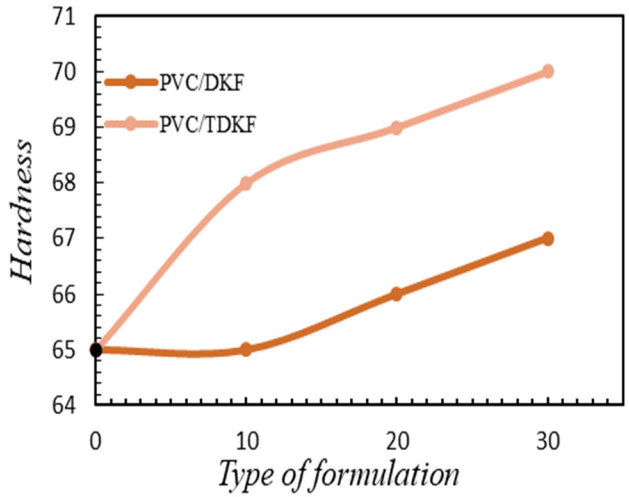

Figure 3. Hardness of PVC and PVC/DKF and PVC/TDKF composites with 10, 20 and 30% load.

3.4 Tensile test

3.4.1 Tensile strength

After chemical treatment with DKF, a decrease in stress was observed for all three formulations compared to composites prepared with DKF. This can be attributed to the degradation of the cellulose during acetylation, which subsequently results in depolymerisation of the cellulose and a loss of crystallinity leading to a drop in its mechanical properties [5, 11]. The problems of cellulose degradation after chemical modification are commonly described in the literature and are problematic when cellulose is used as a reinforcement in composite materials [12]. Another point to note is that the conditions used (temperature, reaction time and swelling agent) can themselves lead to fiber degradation [11]. This result is similar to that found by Luz et al. [13], who recorded a decrease in the tensile strength of PP/cellulose composites from 26.2 to 24.5 MPa and from 25.8 to 20.1 MPa for a filler content of 10 and 20% respectively, after acetylation. This result was attributed to the shape and size of the fibers obtained after chemical modification, as the fibers before acetylation had a fibrous appearance, whereas acetylation resulted in globular and amorphous particles.

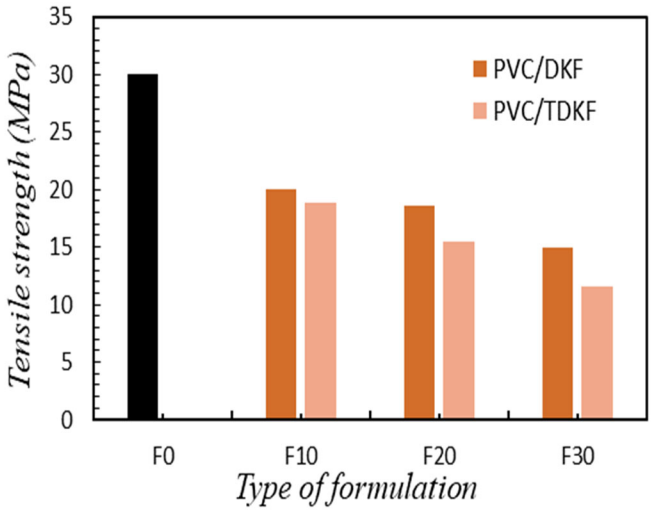

Figure 4. Tensile Strength of PVC and (PVC/DKF and PVC/TDKF) composites for different formulations.

3.4.2 Young's Modulus

Figure 5 shows the evolution of the Young's modulus of PVC and PVC/FNDB and PVC/FNDT composites with 10, 20 and 30% filler. Generally speaking, it can be seen that the introduction of filler into the PVC matrix significantly increases the stiffness of the composites. In fact, composites elaborated with treated and untreated date kernel flour record higher Young's moduli than PVC.

A comparison of the Young's moduli of the different composites shows that incorporating treated date stone flour into PVC results in an increase in Young's modulus compared with composites prepared with untreated flour. Similar results have been found by several researchers. Abdul Khalil et al [14] studied the evolution of the Young's modulus of polyester/coir fibre composites and recorded an increase in this parameter after acetylation of the coir fibres. They explained this result by an improvement in adhesion between the fibres and the polyester matrix due to acetylation. Indeed, the fibre is made more hydrophobic by such a modification and it can be used to prevent delamination at the interface of the fibre with the polyester matrix.

Kalaprasad et al. [15] reported a 14.89% increase in Young's modulus of polyethylene/sisal/glass fibre hybrid composites after chemical modification of these fibres with acetic acid. This result is attributed to the increased hydrophobicity of sisal after treatment.

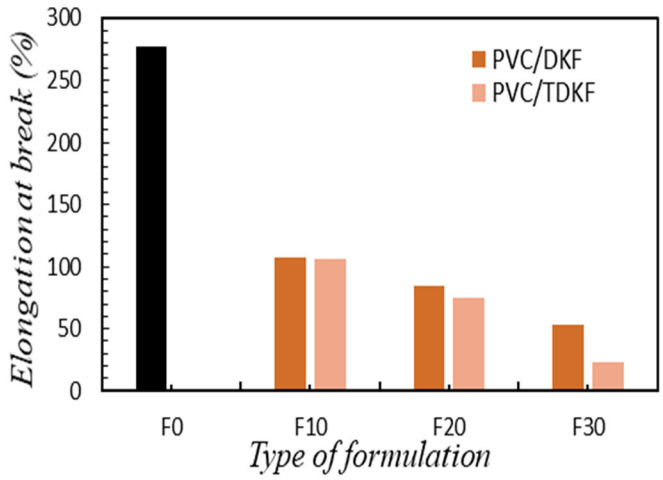

Figure 5. Young's Modulus of PVC and (PVC/DKF and PVC/TDKF) composites for different formulations.

3.4.3 Elongation at break

Figure 6 illustrates the trend in elongation at break for PVC and PVC/DKF and PVC/TDKF composites with 10, 20 and 30% load. It can be seen that the trend for all the formulations as a function of the type and level of filler is characterised by a significant drop in elongation compared with virgin PVC. As for elongation, it falls from 277.55% for PVC to 107.69% and 106.57% for PVC/ DKF and PVC/ TDKF composites (10% filler) respectively.

Comparing the results for the elongation at break of the different composites, it can be seen that acetylation of date stone flour did not affect the elongation at break of the composites at 10% load. However, for the composites loaded with 20% and 30% TDKF, a slight decrease was recorded compared with the composites loaded with DKF, with elongation falling from 52.92% to 22.76% for the PVC/DKF and PVC/TDKF composites (at 30%) respectively. This result is similar to that found by Abdul khalil et al [14], who found that acetylated coir fibres show a decrease in elongation compared to unmodified fibre for the same loading ratio. They explained this decrease by improving fibre-matrix adhesion (to give composites greater stiffness) or because acetylated fibres are more brittle after acetylation.

Vinod et al [16] studied the elongation at break of composites filled with chemically treated Ziziphus mauritiana fibres and found lower values than those prepared with untreated fibres. They explained this result by the better hardness and stiffness obtained thanks to the strong adhesion between the treated fibre and the rubber matrix. Higher extension is obtained from low interfacial adhesion as seen for untreated composites.

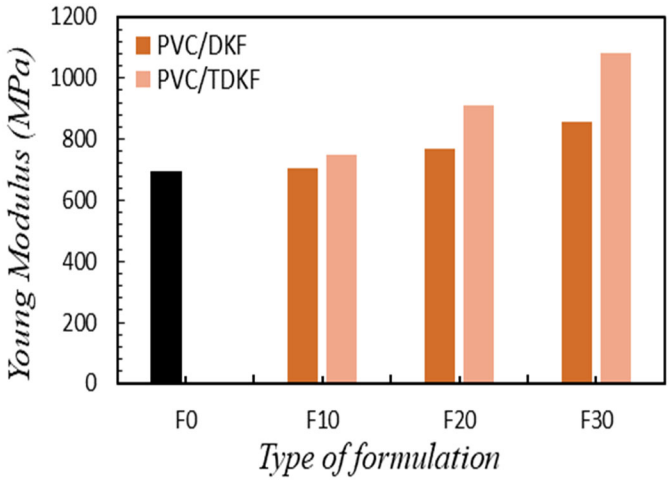

Figure 6. Elongation at break of PVC and (PVC/DKF and PVC/TDKF) composites for different formulations.

4. Conclusion

The analysis of the various experimental results has enabled us to draw the following main conclusions:
Characterization of PVC/NDF composites
- Acetylation of DKF did not affect the density of composites at low loading rates (10% and 20%) compared with composites prepared with untreated flour; however, a decrease in density was recorded for loading rates of 30%.
- The study of mechanical properties showed that:
- The stress and elongation at break of PVC/DKF composites decreased with increasing filler content compared with virgin PVC. These two properties also decreased for PVC/TDKF composites compared with those prepared with DKF.
- The Young's modulus of the composites increased with increasing filler content. An improvement in this property was recorded after chemical treatment with DKF.
- The hardness of the composites increased after acetylation of DKF.

References

[1] M. King, B. Zhu, S. Tang. Mobile. Robot **8** (2001) 520-531.
[2] H. Zegeye, D. Teketay, E. Kelbessa. Nat. Resou. **5** (2014) 864-875.
[3] A. Ari, M Karahan, H.A.M. Ahmed, O. Babiker, R.M.A. Dehşet. AATCC J. Res **10** (2023)163-183.
[4] S. Cichosz, A. Masek, A. Rylski. Materials **13** (2020) 5519.
[5] X. Li, L.G. Tabil, S. Panigrahi. J. Polym. Environ **15** (2007) 25-33.
[6] M. Khali, Z. Boussena, L. Boutekrabt. Rev. Nat. Technol **7** (2015) 15-25.

[7] S. Sahi, H. Djidjelli, S. Touazi, Am Boukerrou. Mater. Tech **109**, (2021) 102.
[8] M.R. Rahman, M.M. Huque, M.N. Islam. Compos. -A: Appl. Sci. Manuf **39**, (2008) 1739-1747.
[9] M.N. Islam, M.R. Rahman, M.M. Huque. Compos. -A: Appl. Sci. Manuf **41** (2010) 192-198.
[10] M.J. John, B. Francis, K.T. Varughese. Compos. -A: Appl. Sci. Manuf **39** (2008) 352-363.
[11] K.Y. Lee, A. Delille, A. Bismarck. Cellulose fibers: bio-and nano-polymer composites (2011)155-178.
[12] D. PASQUINI, M.T. DE Eliangela, S.C. DA, A. Aprigio. Compos. Sci.Technol **68** (2008) 193-201.
[13] S.M. Luz, J.D. TIO, G.J.M. Rocha. Compos. -A: Appl. Sci. Manuf **39** (2008) 1362-1369.
[14] H.P.S. Abdul Khalil, H.D. ROZMAN, M.N. AHMAD. Polym-Plast. Technol. Eng **39** (2000) 757-781.
[15] G. Kalaprasad, B. Francis, S. Thomas. Polym. inter **53** (2004) 1624-1638.
[16] A. Vinod, R. Vijay, D.L. Singaravelu, A.S. Khan, S. Siengchin, F. Verpoor, K.A. Alamry, A.M. Asiri, 2022. J. Indus. Text **51** (2022) 2444-2466.

Journal of Physical & Chemical Research

Journal homepage: https://ojs.univ-bba.dz

Adsorption of humic acid from aqueous solutions on organo Mg-Fe-SDS

Katiba Bouarouri[1], Sabrina Khenchlaoui[2], M Wahib Naceur[3].

[1] Environmental engineering department,faculty of mechanical engineering and process engineering,USTHB. Laboratoire Eau, Environnement, et Developpement Durable (2E2D).Algeria

[2] Environmental engineering department,faculty of mechanical engineering and process engineering,USTHB.Algeria

[3],Chemical Engineering Department, Saad Dahlab University, BP 270 Blida, Algeria. Laboratoire Eau, Environnement, et Developpement Durable (2E2D).Algeria

[1] Corresponding author: Email : katiba_bouarouri@yahoo.fr.

Article history

Received March 3, 2025

Accepted for publication April 22, 2025

Abstract

In this study, Organophilic LDH was prepared by interposing a surfactant (sodium dodecylsulfate, SDS 0.1 M) and applied for the removal of humic acid from solutions in batch system, the synthesized adsorbent (Mg-Fe-SDS) was characterized by FTIR, X-ray diffraction, and BET. Several adsorption kinetics models (pseudo-first order, pseudo-second order, n^{th}-order and intraparticule diffusion) were tested against the experimental results. The calculation of the corresponding parameters show that results are best fitted with n^{th}-order ($n \in R^{+}$), $n \neq 1$model with a determination coefficient close to 1 and a relatively small root mean square error. Among the available mathematical models used to describe the isotherms experimental results (Langmuir, Freundlich and many-parameters models). The three models that are proposed show a better performance than Freundlich, Langmuir. The calculation of the parameters of the different adsorption models was performed on MATLAB using genetic algorithms. Thermodynamic analysis of sorption isotherms suggest that sorption process of humic acid is spontaneous ($\Delta G° < 0$), with a positive enthalpy variation, characteristic of an endothermic process.

Keywords: ZnS; doped, co-doped, FP-LAPW, GGA+mBJ

I. Introduction

Humic acids have a strong effect on the properties of natural water since they represent most of the dissolved organic matter with 50% to 90% of dissolved organic carbon [1].These molecules affect the taste and color of water [2], and represent a source of nutrients to bacteriaand trap heavy metals, pesticides and herbicides [3]. Recent use of anionic clays (layered double hydroxides (LDH)) as adsorbents showed a particular interest for the elimination of micro-pollutants [4]. LDH have a brucite layer structure where the brucitic layers ($M_{II}(OH)_2$) are positively charged. This is due to the partial substitution of bivalent cations M^{II} by trivalent cations M^{III} [5]. Electroneutrality is ensured by anionic species, which are solvated by water molecules present in sheets interspace [4]. The insertion of anionic surfactants modifies the hydrophilic property of the clay which becomes hydrophobic and capable of adsorbing organic pollutants [6]. In the present work, SDS based organophilic LDH, calcined at 773 K are used for the elimination of humic acid. A particular interest is given to the investigation of kinetic and thermodynamic equilibrium as well as adsorption thermodynamics to provide a description of the fixation mode using recently proposed multi-parameters adsorption models.

2. Method

2.1 Materials

Sodium dodecylsulfate (SDS, 0.1 M), HCL (0.1 M), NaOH (0.1 M), $MgCl_2 \cdot 6H_2O$, Na_2CO_3, and $FeCl_3 \cdot 6H_2O$. All reactants from Panreac Qimica SA Castellar del Valles Barcelona, Espana.

2.2 Preparation of humic acids

Commercially available humic acid (Acros) is used in the experiments. A solution with a concentration of 1 g/L
is prepared by dissolving 1 g of humic acid in 62.5 mL of NaOH solution (2 N), followed by addition of distilled water to obtain 1l of solution. The latter is mixed during 24 h then filtered through a 45 µm filter and finally protected from light and kept at a temperature of 277 K [7].

2.3 Synthesis of Mg–Fe–CO_3 phase

Mg–Fe phase with a ratio of Mg/Fe = 2 was prepared by adding a basic solution of NaOH (2 M) and Na_2CO_3 (1 M) to a mixture of two salts, namely $MgCl_2 \cdot 6H_2O$ (0.66 M) and $FeCl3 \cdot 6H_2O$ (0.33 M). Optimum parameters that would lead to crystallized LDH consist of pH = 10, a temperature of 298 K, and a mixing time of 6 h. The resulting suspension is mixed overnight to enhance material crystallization followed
by washing, drying at 338 K, and grinding to obtain Mg–Fe–CO_3.

Subsequently, LDH are calcined at 773 K
during 5 h to improve structural properties and texture, then a decarbonation and dehydration to obtain Mg–Fe–C
with enhanced anionic exchange properties [8].

2.4 Preparation of organophilic LDH

Calcined LDH were added to a solution of surfactant, namely sodium dodecylsulfate (SDS, 0.1 M) with solid to solution ratio equal to 1 g/50 mL. The mixture constantly mixed and heated up to 338 K in an oil bath, while maintaining nitrogen reflux to minimize CO_3^{2-} amount in the solution [9]. The resulting solid is washed five times with distilled water, then dried at 338 K and grinded to obtain Mg–Fe–SDS.

2.5 Adsorption kinetics of humic acid

The investigation of the kinetics of adsorption of a component onto an adsorbent enables to assess the influence of contact time on the adsorbed quantity (Eq. (1)). The main objective of this research is to evaluate the time necessary to reach adsorption equilibrium for different concentrations. All results obtained are reported on a $Q_t = f(t)$plot with:

$$Q_t = \frac{(C_0 - C_t)V}{m} \qquad (1)$$

where $C_o$is the initial concentration fo humic acid AH (mg/L), $C_t$is the residual concentration at time t (mg/L), $V$is the volume of the aqueous solution (L) and m the mass of clay. (g).

2.6 Adsorption isotherm

Adsorption isotherms are drawn at room temperature using suspensions with 10 mg of adsorbent in 10 mL solutions with increasing humic acid concentration. The suspensions with pH = 5 are agitated during 6 h then centrifuged.
The total equilibrium concentration of humic acid (Ce) is measured from the supernatant. where C_0 is the initial concentration of humic acid (mg/L), Ce is the residual equilibrium concentration (mg/L), V is the volume of the aqueous solution (L), and m is the mass of clay.

$$Q_e = \frac{(C_0 - C_e)V}{m} \qquad (2)$$

2.7 Effect of pH on adsorption

pH represents an important parameter for the adsorption process. It affects the charge of the adsorbent surface and the ionization of different functional groups as well as the adsorbate. The investigation of humic acid adsorption onto materials in seawater is carried out under pH values between 2 and 12. A mass of 10 mg of each material is added to 10 mL of solution with an initial concentration of 10 mg/L.

3. Characterization

Diffractograms of Mg-Fe-CO_3 sample, before calcination, after calcination and after exchange by SDS are represented in figure 1. X-ray diffraction results for Mg-F-CO_3 are typical of those of LDH structures encountered in the literature [10]. These symmetrical peaks at *(003)*,*(006)* and *(009)*,as well as asymmetrical at *(015)*, *(018)*, *(110)* and *(113)* indicate that our product is crystallized and similar to those reported in the literature [10]. Mg-Fe-C shows that calcination modifies the crystalline structure of LDHs by causing dehydration, dihydroxylation and decarboxylation. Mixed oxides of MgO type are also formed at 2θ= 42, 93° and 62, 22°. These oxides, which are formed after calcination, are weakly crystallized and exhibit peak broadening on the XRD diagram in accordance with available literature [11]. After intercalation of SDS surfactant (figure 1), the crystalline structure reappears (memory effect) and shows characteristic peaks that correspond to initial LDH reflections.

Mg-Fe-CO3 diagram (figure 2) shows a wide band at ~3440 cm-1, which corresponds to a stretching vibration of lamellar hydroxide groups bonded to different metals [10, 12]. A small vibration band observed at ~3000 cm-1corresponds to the stretching of water molecules [13].A vibration band, observed at ~1630 cm-1, can be attributed to the deformation of interposed water molecules [12]. A vibration band around 1353 cm-1corresponds to asymmetric stretching of interlamellar carbonates (CO3-2) [10, 11]. Vibration bands in the range 800-500 cm-1are attributed to valence vibrations of Mg-O, Fe-O [11]. The presence of SDS ions in the interfoliar space is represented by the two peaks at ~2909 and ~2844 cm-1for the Mg-Fe-SDS phase. These two peaks characterize both symmetric and asymmetric stretching of C-H bond that belongs to the linear chain of interposed SDS. The presence of sulfonate groups at ~105(S=O) asymmetric) and~1193 cm-1 (ν (S=O) symmetric) is also noticeable [15].

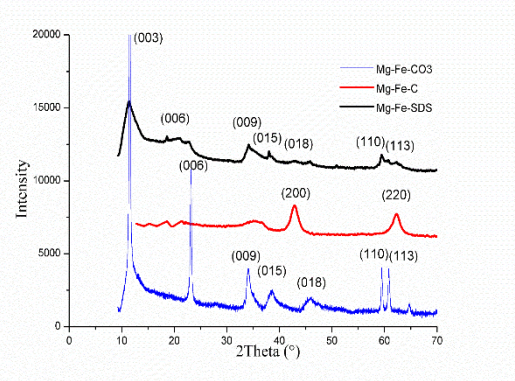

Figure 1. XRD diagrams: Mg-Fe-CO_3, Mg-Fe-C and Mg-Fe-SDS.

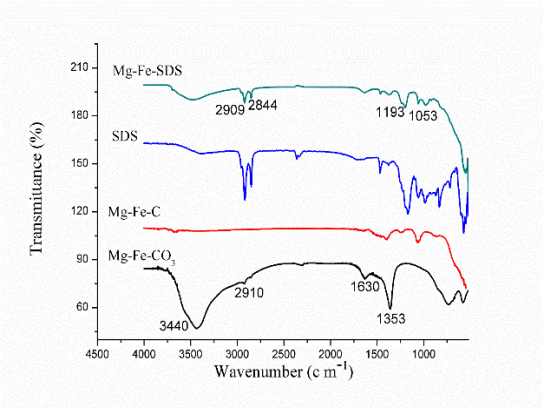

Figure 2.IR spectra of anionic clays.

Table 1. Constants of adsorption kinetics models on different materials (C_0= 10 mg/L, T =298 K , pH =5).

Models	Parameters	Mg-Fe-SDS			Mg-Fe-C			
		Initial concentrations (mg/l)						
		10	30	100	10	30	50	90
Pseudo-first-order model $q_t = q_e(1 - e^{-k_1 t})$	Q_e (cal) (mg/g)	9	30	90	8	28	42	70
	RMSE	0.7268	1.6112	7.6039	0.3708	2.5974	2.5793	2.4560
	r^2	0.9354	0.9853	0.9332	0.9879	0.9435	0.9677	0.9896
	k_1 (min^{-1})	0.2100	0.1611	0.0763	0.0798	0.0899	0.1116	0.1349
Pseudo-second-order model $Q_t = \frac{k_2(Qe)^2 t}{1 + k_2 Q_e t}$	Q_e(cal) (mg/g)	8.66	29.85	88.78	7.88	27.63	41.72	69.62
	RMSE	0.3848	0.7559	3.6864	0.0811	1.4311	1.0807	0.9457
	r^2	0.9771	0.9944	0.9765	0.9990	0.9768	0.9917	0.9976
	k_2(g/mg/min)	0.0505	0.0143	0.0017	0.0173	0.0056	0.0073	0.0055
n-order model	Q_e(cal) (mg/g)	8.26	29.35	87.59	7.88	26.69	41.59	69.58

$Q_t = 1 - (1 + (n-1)k_n t)^{\frac{1}{1-n}}$	*RMSE*	0.1619	0.4090	3.2931	0.0809	0.8875	1.057	0.9420
	r^2	0.9936	0.9977	0.9804	0.9990	0.9885	0.9920	0.9977
	k_n	1.7028	1.7895	0.1992	0.1370	0.3451	0.3752	0.3601
	N	3.2940	2.9355	2.3430	1.9864	2.8749	2.1545	1.9428

3.2 Adsorption isotherm

By adjusting the experimental points on the different new models proposed with several parameters, and based on the values of the coefficient r2 and RMSE, it appears that the values of the coefficient of correlations r2 approaches unity and the RMSE tends towards zero, which clearly shows the precision of the models proposed compared to the Freundlich and Langmuir models. We also note that the adsorption process of HA on different materials is better presented by the proposed model (03) with four parameters. Curves of figure 4 shows the fitting of experimental data with these different models. The adsorption process of humic acid is well represented by the four parameters mode. Parameters calculation was performed on MATLAB using genetic algorithms.

Table .2. Constants of adsorption isotherms of humic acid.

Modèles		Paramètres	Mg-Fe-SDS	Mg-Fe-C
Freundlich	$Q_e = Qm\ aC_e^n$	RMSE	18,6165	12,6418
		r^2	0,9322	0,9708
		a	0,1279	0,0755
		n	0,5418	0,5933
		Qe cal (mg/g)	256,139	203,35
Langmuir	$Q_e = \frac{Q_m a C_e}{1+aC_e}$	RMSE	21,0740	20,2892
		r^2	0,9561	0,9715
		a	0,0947	0,0568
		Qe cal (mg/g)	198,28	161,035
Proposed model 01		RMSE	3,6666	5,2482
		r^2	0,9977	0,9951
$Q_e/Q_m = (1-\exp(-aCe^2))^{1/2}$		a	0,0029	$7{,}733.10^{-0,4}$
		Qe cal (mg/g)	231,15	183,30

Proposed model 02 $Qe/Qm=b\ (1-\exp\ (-aCe^2))^{1/2}$	RMSE	3,6664	5,1180
	r^2	0,9977	0,9953
	a	0,0029	0,0008
	b	1,0004	0,9873
	Qe cal (mg/g)	239,53	185,43
Proposed model 03 $Qe/Qm=b\ (1-\exp\ (-aCe^n))^m$	RMSE	2,1904	2,9572
	r^2	0,9991	0,9983
	a	0,0277	3,3015
	b	0,9960	1,2528
	n	1,3922	0,1558
	m	0,9456	164,883
	Qe cal (mg/g)	238,68	185,33
	Qe exp (mg/g)	238,92	185,28

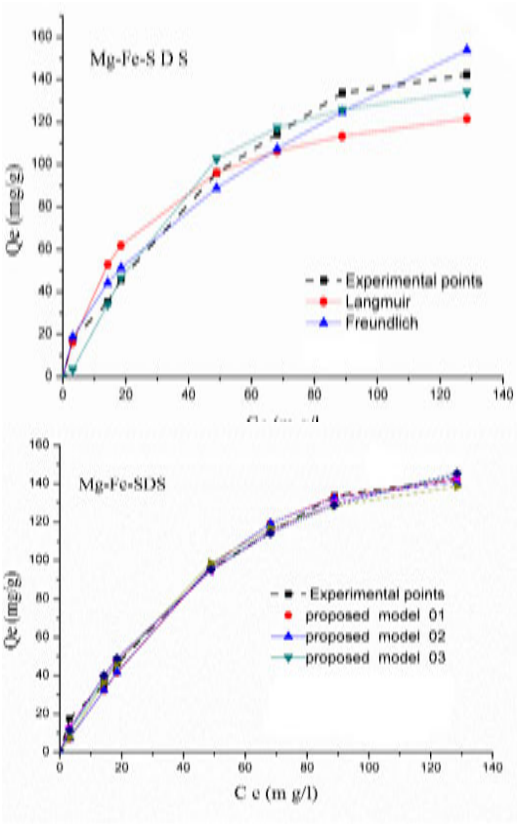

Figure 4. Adsorption isotherms (t =5 h, T = 298 K and C_0=10 mg/L).

3.3 Calculation of thermodynamic parameters

Values of free energy ΔG_{0ads} reported in Table (III), suggest that the process is spontaneous while positive values of enthalpy ΔH_0 shows that the process is endothermic favored by increasing temperature fig.5. Positive values of entropy ΔS_{0ads} show that LDH-adsorbate system is less ordered that the molecules [11].

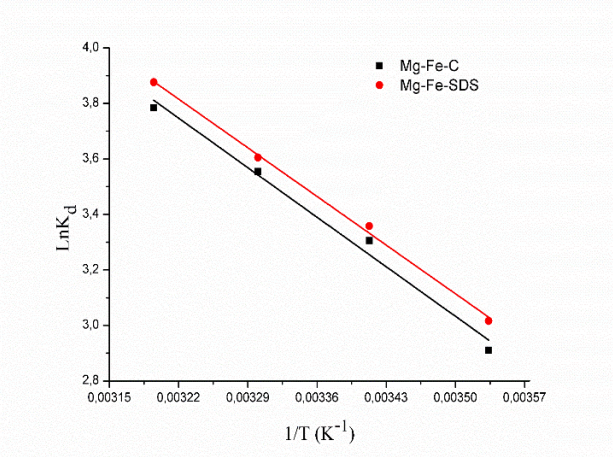

Figure 5. Van't Hoff plot for different materials.

Table 3 Thermodynamic parameters ΔH_0, ΔS_0 and ΔG_0 related to the adsorption of Mg-Fe-SDS.

Samples	Temperature (K)	ΔG° (kJ/mol)	ΔH° (kJ/mol)	ΔS° (kJ/mol k)
Mg-Fe-SDS	283	-22.48	56.91	270.99
	293	-25.19		
	313	-27.90		

4. Conclusion

Materials characterization confirmed successful synthesis of LDHs. Results of infrared spectra showed LDH characteristic bands with carbonate anions interposed in the interlamellar spacing. Thermal treatment confers to the material a relatively high specific surface. SEM and XRD characterization results show that LDH are crystalline. This crystalline structure reappears (memory effect) after interposing SDS surfactant in LDHs with characteristic peaks that correspond to initial LDH reflections with a slight modification of crystallinity. Results show that

pseudo-first order kinetic model is valid at early stages of the adsorption process, while the pseudo-second order model gives better results. However, the best fit of the experimental results was obtained using the n-order model (n €R^+) with a determination coefficient close to one. Models of adsorption isotherms that were proposed, particularly 3 parameters model, give better results than classical Freundlich and Langmuir models. A thermodynamics analysis enabled the calculation of enthalpy, entropy and free energy of adsorption and showed that the adsorption process is chemical, spontaneous and endothermic.

5. References

[1] Y. Zhang, X.Zhang, Y. Song, J. Wang, Enhanced performance of calcium-enriched coal ash for the removal of humic acids from aqueous solution, Fuel 141 (2015) 93–98.
[2] M.S. Gasser, H.T. Mohsen, H.F. Aly,Humic acid adsorption onto Mg/Fe layered double hydroxide, Colloids and Surf A: Physicochem. Eng. Aspects 331 (2008) 195–201.
[3] T.S. Anirudhan, M. Ramachandran, Surfactant-modified bentonite as adsorbent for the removalofhumic acid from wastewaters, Appl. Clay. Sci. 35 (2007) 276–281.
[4] K. Morimoto, Determination and reduction of Fe (III) incorporated into Mg–Fe layered double hydroxide structures, Appl. Clay Sci 121–122 (2016) 71–76.
[5] I.M. Ahmed, M.S. Gasser, Adsorption study of anionic reactive dye from aqueous solution to Mg–Fe–CO_3layered double hydroxide (LDH), Appl. Surface .Sci 259 (2012) 650– 656.
[6] M. Cruz-Guzman, R. Celis,M.C. Hermosin,J. Cornejo, Adsorption of the herbicide sinezine by montmorillonite modified with neutral organic cations. Environ. Sci. Technol. 38(2004)180–186.
[7] F. Zermane, M.W. Naceur, B. Cheknane, N. Ait Messaoudene, Adsorption of humic acids by a modified Algerian montmorillonite in synthesized seawater, Desalination, 179 (2005) 375–380.
[8] W.T. Reichle, Synthesis of anionic clay minerals (mixed metal hydroxides hydrotalcite), Solid State Ionics, 22 (1986) 135–141.
[9] Y. You, H. Zhao, G.F. Vance, Surfactant-enhanced adsorption of organic compounds by layered double hydroxides, Colloids Surf., A, 205 (2002) 161–172.
[10] Y. Guo , Z. Zhu , Y. Qiu , J. Zhao, Enhanced adsorption of acid brown 14 dye on calcined Mg/Fe layered double hydroxide with memory effect, Chem.Eng .J. 219 (2013) 69–77.
[11] N. Benselka-HadjAbdelkader, A. Bentouami, Z. Derrich, N. Bettahar, L. C. de Ménorva,Synthesis and characterization of Mg–Fe layer double hydroxides and its application onadsorption of Orange G from aqueous

solution, Chem. Eng .J. 169 (2011)231–238.
[12] Hideaki Murase, H. Yasuda , A.Nakahira, Effect of high magnetic field on ferrite materials obtained by calcination of layered double hydroxide, Materials Transactions 48 (2007) 2877-2882.
[13] M.J. Reis, F. Silverio, J. Tronto, J.B. Valim, Effects of pH, temperature, and ionic strength on adsorption of sodium dodecylbenzenesulfonate into Mg–Al–CO_3 layered double hydroxides, J. Phys. Chem. Solids 65 (2004) 487–492.
[14] F.P.Jiao, L. Shuai, J.G. Yu, X.Y Jiang, X.Q. Chen, S.L. Du, Adsorption of glutamic acid from aqueous solution with calcined layered double Mg−Fe−CO_3 hydroxide, Trans. Nonferrous Met. Soc. China 24(2014) 3971−3978.
[15] L. D. L. Miranda, C. R. Bellato, M. P.F. Fontes, M. F. de Almeida, J. L. Milagres, L. A.Minim, Preparation and evaluation of hydrotalcite-iron oxide magnetic organocomposite intercalated with surfactants for cationic methylene blue dye removal, Chem. Eng.J.254 (2014) 88–97.

J. Phys. &Chem. Res. 4, Issue 1, June (2025) 31–36

Journal of Physical & Chemical Research

Journal homepage: https://ojs.univ-bba.dz

Numerical Study of lead-free halide perovskites solar cells using Efficient materials as electron transport materials

Souad Belferdi[1]*, Mohamed Cherif Okba[2], Mokrani Sabrina[3], Abdi Mohamed Amir[1], Bencherif Hichem[1].

[1]LEREESI, Laboratory, HNS-RE2SD, Batna 05000, Algeria.
[2](LREEI), Faculty of Hydrocarbons and Chemistry University M'hamed Bougara of Boumerdes (UMBB).
[3]LEA, Electronics Department, University Mustafa Benboulaid, Batna 2 − 05000, Algeria
** Corresponding author: Tel.:0561411202,0661171163,0674821363,0541042877; E-mail address: s.belferdi@hns ,re2sd.dz, AMIR.ABDI@hns-re2sd.dz, bencherif.hichem@hns-re2sd.dz, sabrina.mokrani@univ - batna2.dz*

Article history
Received February 25, 2025
Accepted for publication April 24, 2025

Abstract

This work presents a comprehensive theoretical analysis aimed at finding the elements that impede the efficiency of KGeCl3 solar cells. The aim of our investigation is to examine the impact of various characteristics to enhance its performance. The improved design exceeds the baseline, attaining a JSC of 37.08 mA/cm², Voc of 0.77 V, and FF of 60.80%, therefore indicating the possibility to reach an efficiency of up to 17.57% by the strategic optimization of 2D materials as the electron transport layer (ETL). The suggested analysis facilitates the identification of relevant degradation components and creates a basis for further design optimization. showcasing the effectiveness of our approach, the findings from this study not only highlight the critical factors affecting 2D perovskite solar cell performance but also provide a foundation for future research and optimization efforts.

Keywords: 2D materials; Solar cells; Simulation; optimization

1. Introduction

Two-dimensional materials have emerged as a prospective frontier in solar cell technology, providing distinctive benefits such as customizable optoelectronic properties and enhanced stability[1-4] However, despite their potential, 2D materials solar cells face several challenges that impact their overall efficiency [5]. Addressing these challenges requires a detailed understanding of how various factors influence the performance of these cells. The efficiency of KGeCl3 perovskite solar cells is influenced by a complex interplay of parameters, including material composition, layer thickness, and fabrication techniques [6]. These factors collectively affect key performance indicators such as short-circuit current density (JSC), open-circuit voltage (Voc), and fill factor (FF). Understanding and optimizing these parameters is essential for enhancing the overall efficiency of the solar cells.This paper presents a comprehensive theoretical analysis aimed at identifying the factors that limit the efficiency of 2D perovskite solar cells. Our approach involves a detailed examination of how different design parameters affect cell performance and the development of optimization strategies to improve efficiency. Through this analysis, we demonstrate that strategic adjustments to the properties of 2D materials can lead to significant improvements, achieving a JSC of 37.57% mA/cm², Voc of 0.77 V, and FF of 60.80%. This optimization results in a potential efficiency of up to 17,57%, showcasing the effectiveness of our approach.

2. Device structure

In our study we utilized a IZO/ TMCs/KGeCI3/Cu2O thin film solar cell configuration, where IZO as the transparent oxide layer, KGeCI3 acted as the absorber layer, MoS2 as the emitter, and Cu2O as hole transport layer,were set at 0.2 µm, 0.5 µm, 0.02 µm and 0.02 µm, respectively.as represente in Figure1. to verify the precision of our proposed model using scaps 1D simulation, The material parameters for modeling were meticulously chosen based on existing data from the literature based on experimental and DFT calculations, as illustrated in Table 1.

3. Modeling framework

SCAPS-1D is a sophisticated simulation tool designed to provide precise insights into the performance of semiconductor devices. It carefully incorporates a range of parameters including defect density, layer thicknesses, carrier concentrations, metal work functions, and the properties of the back hole transport layer (HTL). By solving the fundamental governing equations—such as the Poisson equation and the continuity equations for electrons and holes—SCAPS-1D accurately models the complex behavior of semiconductor structures, as detailed in Eqs (1)-(3). This advanced software is crucial for analyzing and optimizing the performance of our solar cell architecture [11].

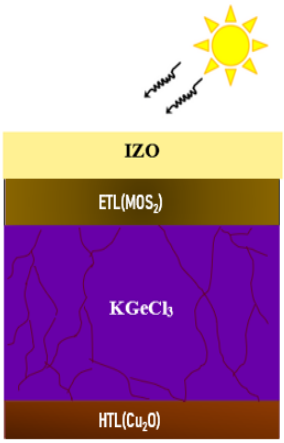

Figure 1. KGeCl3 perovskite solar cell structure

	TCO	ETL	PAL	HTL
Parameters (units)	IZO	MoS2	KGeCl3	Cu2O
Thickness (µm)	0.02	0.02	0.5	0.2
Bandgap (eV)	3.5	1.29	1.1	2
Electron affinity (eV)	4.5	4.2	4	3.8
Dielectric permittivity (relative)	10	4	23.01	10
Effective densityof states (cm-3)CB	$1*10^{19}$	2.2*1018	$6.81*10^{18}$	$3*10^{18}$
effective density of states (cm-3)CV	$1*10^{19}$	$2.2*10^{18}$	$3.45*10^{18}$	$3*10^{19}$
Electron mobility (cm^2/Vs)	10-2	50	92.92	$3.7*10^2$
Hole mobility (cm^2/Vs)	10-3	30	68.59	10^7
Acceptor concentration, NA(cm-3)	0	0	10^{15}	10^{17}
Donor concentration, ND(cm-3)	$1*10^{18}$	$1*10^{18}$	109	0

Table 1. Input parameters values [7-10]

$$\frac{\partial}{\partial x}\left(\varepsilon_0 \varepsilon_R \frac{\delta \psi}{\delta x}\right) = -q\left(p - n + N_d^+ - N_A^- + \frac{\rho_{def}}{q}\right) \quad (1)$$

$$-\frac{\partial J_n}{\partial x} - R_n + G = \frac{\partial n}{\partial t} \quad (2)$$

$$-\frac{\partial J_p}{\partial x} - R_p + G = \frac{\partial p}{\partial t} \quad (3)$$

In this analysis, we explore the underlying physics of our solar cell by investigating essential parameters and equations, each represented by specific symbols to denote various physical quantities. The electrostatic potential is denoted by ψ, while ε0 represents both the relative permittivity of the semiconductor and the permittivity of free space. The concentration of free carriers is represented by p for holes and n for electrons. The densities of ionized acceptors and donors are denoted by NA− and ND+, respectively. Additionally, ρdef indicates the density of defect charges. The rate of photo-generation within the cell is symbolized by G, and R represents the net recombination rate.

4. Results and discussion

Figure 2(a) illustrates the I-V characteristics that were generated the KGeCI3 with MoS2 as ETL show the highest efficiency with 17.58%, as evidenced by the reduced values of defects in the absorber layer and interface. This device's current density is high, and its VOC is 0.77 v, as shown in the figure. Figure 2 (b) illustrates the quantum efficiency of the structure that was attained. The quantum efficiency (QE) ranging from 450 to900 nm is 90 percent. Thereafter, the QE decreases to 89 percent due to the narrow band gap of the perovskite, which did not absorb in the visible spectrum. However, the QE reaches zero at a wavelength greater than 900 nm, as this wavelength falls below the absorber layer bandgap.

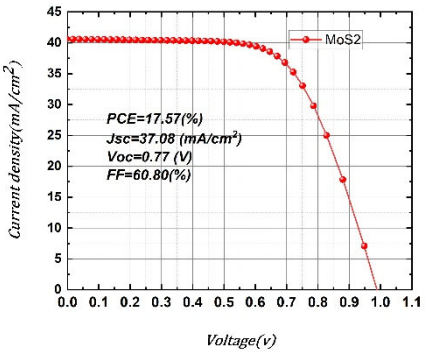

Figure 2. IV curve

5. Effect of ETL doping

Figure 5 illustrates the impact of the doping concentration in the ETL layer. The figure illustrates that at minimal donor densities, the power conversion efficiency (PCE) initiates at around 25%. As donor density escalates, the PCE swiftly rises to about 28% within the range of 2×10^{19} to 4×10^{19} cm^{-3}. Upon reaching this juncture, the PCE incrementally escalates at a diminished pace, nearing a peak value of around 29.5% as the donor

density attains 1×10^{20} cm^{-3}, akin to the increase in Voc and FF with increased concentration. This phenomenon mostly results from the improved collecting technique. The donor density significantly affects the power conversion efficiency (PCE), demonstrating an optimal range where efficiency increases considerably, followed by a region where further increases in donor density provide minimal efficiency improvements. In contrast Jsc significantly diminishes at reduced donor densities but stabilizes above a certain threshold, exhibiting a little increase as donor density further escalates. This indicates that an excess of donor atoms may initially hinder current generation, but the impact diminishes with elevated densities.

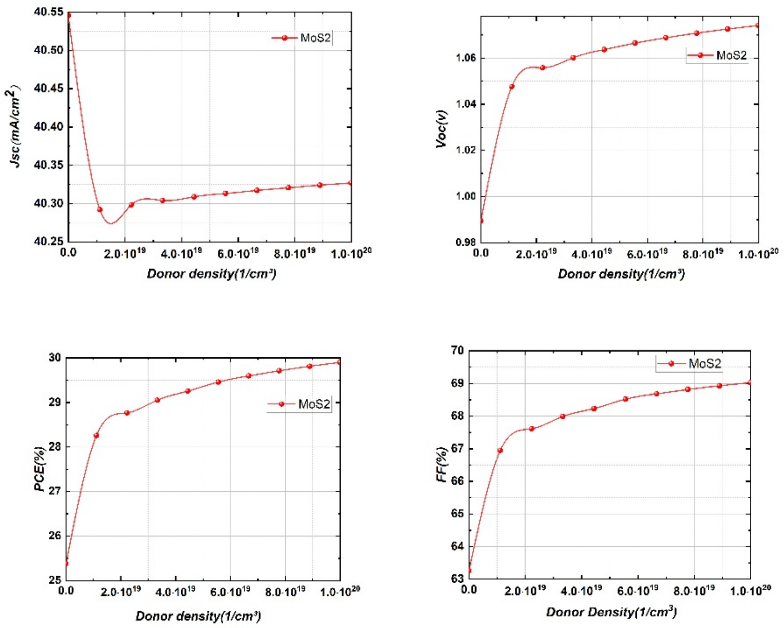

Figure 4. Effect of ETL doping Density

5. Conclusion

This study offers an extensive examination of the efficiency factors in KGeCl3 perovskite solar cells utilizing MoS2 as the electron transport layer, underscoring Doping ETL impact on performance. Through systematic optimization of material characteristics and resolution of interface challenges, we attained significant improvements in solar cell performance. The improved design resulted in a short-circuit current density (JSC) of 37.08 mA/cm², an open-circuit voltage (Voc) of 0.77 V, and a fill factor (FF) of 74.38%, achieving a potential efficiency of 15.49%. The results indicate significant possibilities for enhancements in 2D perovskite solar cells with focue doptimization. Our findings identify

critical elements influencing performance and establish a foundation for future.

References

[1] "pMoS2_nSnS2-In2S3.pdf."
[2] J. Buencuerpo et al., "Efficient light-trapping in ultrathin GaAs solar cells using quasi-random photonic crystals," Nano Energy, vol. 96, p. 107080, Jun. 2022, doi: 10.1016/j.nanoen.2022.107080.
[3] M. Saifur Rahman, K. A. Rikta, L. F. Abdulrazak, and M. S. Anower, "Enhanced performance of SnSe-Graphene hybrid photonic surface plasmon refractive sensor for biosensing applications," Photonics Nanostructures - Fundam. Appl., vol. 39, p. 100779, May 2020, doi: 10.1016/j.photonics.2020.100779.
[4] A. S. R. Bati, M. Batmunkh, and J. G. Shapter, "Emerging 2D Layered Materials for Perovskite Solar Cells," Adv. Energy Mater., vol. 10, no. 13, p. 1902253, Apr. 2020, doi: 10.1002/aenm.201902253.
[5] C. Aumaitre, D. Joly, D. Aldakov, and R. Demadrille, "Alternative Binary and Ternary Metal Oxides for Dye- and Quantum Dot-Sensitized Solar Cells," in The Future of Semiconductor Oxides in Next-Generation Solar Cells, Elsevier, 2018, pp. 85–115. doi: 10.1016/B978-0-12-811165-9.00003-X.
[6] Z. Shi and A. H. Jayatissa, "Perovskites-Based Solar Cells: A Review of Recent Progress, Materials and Processing Methods," Materials, vol. 11, no. 5, p. 729, May 2018, doi: 10.3390/ma11050729.
[7] A. Kostopoulou, I. Konidakis, and E. Stratakis, "Two-dimensional metal halide perovskites and their heterostructures: from synthesis to applications," Nanophotonics, vol. 12, no. 9, pp. 1643–1710, Apr. 2023, doi: 10.1515/nanoph-2022-0797.
[8] H. Abnavi, D. K. Maram, and A. Abnavi, "Performance analysis of several electron/hole transport layers in thin film MAPbI3-based perovskite solar cells: A simulation study," Opt. Mater., vol. 118, p. 111258, Aug. 2021, doi: 10.1016/j.optmat.2021.111258.
[9] C. Li and I. Tlili, "Novel study of perovskite materials and the use of biomaterials to further solar cell application in the built environment: A molecular dynamic study," Eng. Anal. Bound. Elem., vol. 155, pp. 425–431, Oct. 2023, doi: 10.1016/j.enganabound.2023.06.018.
[10] A. Kumar, D. Punetha, and S. Chakrabarti, "Performance optimization of phenylethylammonium-formamidinium tin iodide perovskite solar cell by contrasting various ETL and HTL materials," J. Nanoparticle Res., vol. 25, no. 3, p. 52, Mar. 2023, doi: 10.1007/s11051-023-05702-9.
[11] S. M. Sze and K. K. Ng, Physics of semiconductor devices, 3rd ed. Hoboken, N.J: Wiley-Interscience, 2007.

J. Phys. &Chem. Res. 4, Issue 1, June (2025) 37–42

Journal of Physical & Chemical Research

Journal homepage: https://ojs.univ-bba.dz

Variational quantum Monte Carlo for the harmonium system

Khalfallah Farid[1,2]

[1] Department of Matter Sciences, Faculty of Sciences and Technology, Mohamed El Bachir El Ibrahimi University of Bordj Bou Arreridj 34030, Algeria.

[2] Laboratory of Materials Physics, Radiation and Nanostructures (LPMRN), Faculty of Sciences and Technology Mohamed El Bachir El Ibrahimi University of Bordj Bou Arreridj 34030, Algeria.

** Corresponding author: Tel./Fax: +213662290780; E-mail address: f.khalfallah@univ-bba.dz*

Article history

Received April 17, 2025

Accepted for publication April 30, 2025

Abstract

Relatively good accuracy (< 2%) for intermediate and strong regime for the ground state energy of the harmonium system (Hook's atom) was obtained by variational Monte-Carlo (VMC) calculations. Our study focus on the variation of the ground state energy with respect to the oscillation frequency ω and the balance between the three different part of the energy (kinetic, coulomb and harmonic). Results were compared with several exactly known values of ground state energy for a series of discreet but limited values of the oscillation frequency.

Keywords: Harmonium, VMC, MC integration, Gradient Descent.

1 Introduction

The harmonium quantum system, also called hook's atom, is a model of 2 electrons confined in spherical harmonic potential. Introduced in the 1960s and further developed by Kestner [1] and Kais [2][3], it is an exactly solvable model but only for a certain values of the oscillator frequency ω (Taut [4], Cioslowski [5][6]). It is a benchmark for approximations like

DFT and configuration interaction and serves as a paradigmatic system for studying electron correlation effects in few-body physics. The aim of this paper is to apply VMC calculation to this model and compare with exact results.

2 Method

Schrödinger equation: In atomic units ($\hbar = m_e = ke^2 = 1$), the kinetic energy for the two electrons in the system is given by $T = -\Delta_1/2 - \Delta_2/2$, the harmonic potential energy operator is $V_{HO} = \omega r_1^2/2 + \omega r_2^2/2$, and the Coulomb interaction energy operator between the 2 electrons is $V_{ee} = 1/r_{12}$. The Schrödinger equation then reads:

$$\left(-\frac{1}{2}(\Delta_1 + \Delta_2) + \frac{1}{2}\omega(r_1^2 + r_2^2) + \frac{1}{r_{12}}\right)\psi(\vec{r}_1, \vec{r}_2) = E\psi(\vec{r}_1, \vec{r}_2) \qquad (1)$$

The exact ground state solution is only known for a certain number of discrete frequencies ω_n (representing the roots of polynomials of degree [n/2]) [4]. These ground states are singlet states in witch the antisymmetry of the wave function is captured by the spin part.

Variational calculation: The computation of the ground state involves the minimization of the expectation value of the Hamiltonian:

$$\langle H \rangle = \frac{\langle \psi | H | \psi \rangle}{\langle \psi \mid \psi \rangle} = \langle T \rangle + \langle V_{HO} \rangle + \langle V_{ee} \rangle \qquad (2)$$

We use Gaussian trial wave functions with 2 parameters α_1, α_2 derived from the independent electrons model (where e-e interaction is neglected): $\psi_{\alpha_1}(r_1) = c_1 e^{-\alpha_1 r_1^2}, \psi_{\alpha_1}(r_2) = c_2 e^{-\alpha_2 r_2^2}$. Spin functions are not considered (they factor out and reduce to unity by normalization). The normalized wave function is :

$$\psi_{\alpha_1,\alpha_2}(r_1, r_2) = \left(\frac{4\alpha_1\alpha_2}{\pi^2}\right)^{3/4} e^{-(\alpha_1 r_1^2 + \alpha_2 r_2^2)} \qquad (3)$$

This leads to 6-d spatial integrals, some of which, arising from 1-body terms, are calculated exactly, while others, stemming from the 2-body Coulomb term, are computed numerically with MC integration. Due to these 2-body integrals, the minimization of $\langle H \rangle$ leads to non-explicit equations for (α_1, α_2). We then use the gradient descent method for our optimization.

Monte Carlo Integration: The integrals arising from the e-e interaction term are difficult to evaluate exactly. They are numerically evaluated using

Monte Carlo integration with a probability density function $\rho(\vec{r}_1,\vec{r}_2) = \left|\psi_{\alpha_1,\alpha_2}(\vec{r}_1,\vec{r}_2)\right|^2$. The formula for the expectation value for a sample size of N points allows us to write:

$$\int_D \rho(\vec{r}_1,\vec{r}_2) f(\vec{r}_1,\vec{r}_2) dv_1 dv_2 \simeq \frac{1}{N}\sum_{i=1}^{N} f(\vec{r}_1,\vec{r}_2) \qquad (4)$$

Gradient Descent: This optimization method allows us to calculate the minimum of a function $F(\alpha_1,\alpha_2)$ by following the opposite direction of the local gradient. The calculation of the points $\vec{R}_k(\alpha_{1k},\alpha_{2k})$ uses the iterative formula with step δ_k :

$$\vec{R}_{k+1} = \vec{R}_k - \delta_k \vec{\nabla} F(\alpha_{1k},\alpha_{2k}) \qquad (5)$$

3 Calculations

The exact calculation of the expectation values of the kinetic and harmonic potential energies gives:

$$\langle T\rangle(\alpha_1,\alpha_2) = \frac{3}{2}(\alpha_1+\alpha_2), \qquad \langle V_{Ho}\rangle(\alpha_1,\alpha_2) = \frac{3}{8}\omega^2\left(\frac{1}{\alpha_1}+\frac{1}{\alpha_2}\right) \qquad (6)$$

For the coulomb e-e interaction energy, we obtain the following 6-d integral:

$$\langle V_{ee}\rangle = I(\alpha_1,\alpha_2) = \int_{6d}\left(\frac{4\alpha_1\alpha_2}{\pi^2}\right)^{3/2} \frac{e^{-2(\alpha_1 r_1^2+\alpha_2 r_2^2)}}{|\vec{r}_1-\vec{r}_2|} dv_1 dv_2 \qquad (7)$$

Witch gives:

$$\langle H\rangle = E(\alpha_1,\alpha_2) = \frac{3}{2}(\alpha_1+\alpha_2) + \frac{3}{8}\omega^2\left(\frac{1}{\alpha_1}+\frac{1}{\alpha_2}\right) + I(\alpha_1,\alpha_2) \qquad (8)$$

Then the gradient descent method leads to the iterative equations:

$$\begin{cases} \alpha_{1,k+1} = \alpha_{1,k} - \delta_k\left(\frac{3}{2} - \frac{3}{8}\frac{\omega^2}{\alpha_{1,k}^2} + \frac{3}{2\alpha_{1,k}} I(\alpha_{1,k},\alpha_{2,k}) - I_1(\alpha_{1,k},\alpha_{2,k})\right) & (9) \\ \alpha_{2,k+1} = \alpha_{2,k} - \delta_k\left(\frac{3}{2} - \frac{3}{8}\frac{\omega^2}{\alpha_{2,k}^2} + \frac{3}{2\alpha_{2,k}} I(\alpha_{1,k},\alpha_{2,k}) - I_2(\alpha_{1,k},\alpha_{2,k})\right) & (10) \\ \text{with}: I_{1,2}(\alpha_1,\alpha_2) = \int_{6d}\left(\frac{4\alpha_1\alpha_2}{\pi^2}\right)^{3/2} 2r_{1,2}^2 \frac{e^{-2(\alpha_1 r_1^2+\alpha_2 r_2^2)}}{|\vec{r}_1-\vec{r}_2|} dv_1 dv_2 & (11) \end{cases}$$

4 Results

In the iterative equations (9, 10), the integrals I, I_1, I_2 are evaluated at each step δ_k using Monte Carlo with sufficient precision (sample size $= 10^8$). The convergence of (α_1, α_2) and the optimal energies is achieved after a certain number of steps. This calculation was carried out for a wide range of frequencies ω. The result is shown in the table and figures below.

ω	$\langle T \rangle$	$\langle V_{HO} \rangle$	$\langle V_{ee} \rangle$	$\langle H \rangle$	E (exact [4]	$\Delta E/E$
0.00140	0.00054	0.00817	0.01522	0.02394	0.01831	0.307
0.00189	0.00081	0.00999	0.01854	0.02934	0.02275	0.289
0.00263	0.00125	0.01249	0.02306	0.03681	0.02901	0.268
0.00382	0.00199	0.01647	0.02911	0.04758	0.03823	0.244
0.00584	0.00341	0.02249	0.03807	0.06397	0.05257	0.216
0.00957	0.00637	0.03236	0.05202	0.09076	0.07662	0.184
0.01734	0.01331	0.05084	0.07517	0.13933	0.12142	0.147
0.03653	0.03274	0.09172	0.11791	0.24238	0.21922	0.105
0.1	0.10574	0.21278	0.21179	0.53031	0.5	0.060
0.5	0.63945	0.87965	0.52096	2.04007	2	0.020
1	1.323	1.70068	0.74946	3.77314		:
2	2.93470	3.06674	1.11638	7.11783		:
4	5.625	6.4000	1.54548	13.5704		:
8	11.8952	12.1056	2.24652	26.2474		< 0.02
16	23.9109	24.0893	3.18544	51.1857		:
32	47.6876	48.3144	4.49665	100.498		:
64	95.9655	96.0344	6.38215	198.382		:
128	191.873	192.126	9.02678	393.026		:

Table 1: Optimal values (for the ground state) of the kinetic, coulomb, harmonic, and total energy $\langle H \rangle$ (in Hartree) as a function of the frequency ω. The first ten values correspond to the first ten frequencies for which the exact solution is known.

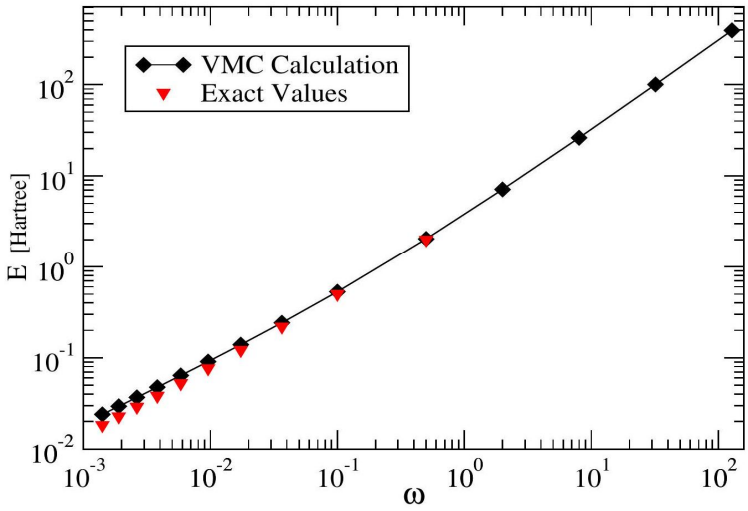

Figure 1: Energy of the ground state of the harmonium system vs frequency ω

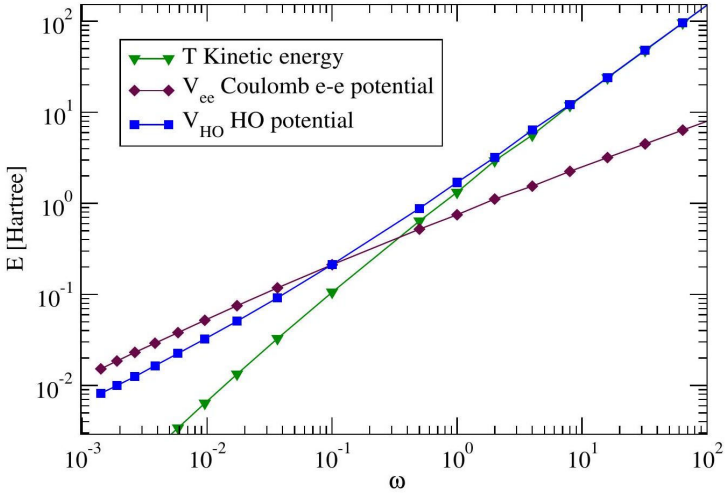

Figure 2: Kinetic, coulomb and harmonic energies for the ground state

5 Discussion

The results of our calculations of the ground state energy of the harmonium (table 1 and figure 1) shows a good accuracy for the variational Monte Carlo method with gradient descent minimization, particularly for the medium and high frequency regime ($\Delta E/E \leq 0.02$ for $\omega \geq 0.5$ a.u. $= 4.13 \cdot 10^{16}$ s^{-1}) despite the use of a simple two parameters Gaussian trial wave function. Indeed, for $\omega = 0.5$ a.u. we obtained $\langle H \rangle = 2.04 E_H$

compared to the exact value $E = 2E_H$. The accuracy then follows an upward trend for high frequencies. It is important to note that at high frequencies, the harmonic and kinetic energies are dominant compared to the Coulomb energy, as shown in figure 2, thus the influence of the latter remains minimal. Around the value $\omega = 0.5$ a.u. the three energies show the same order of magnitude, then the Coulomb interaction between electrons becomes dominant at low frequency (< 0.5 a.u.) where the precision begins to degrade. We can confidently assert that the source of errors primarily stems from the choice of the trial wave function and not from the Monte Carlo integration, which is more than sufficient for this calculation.

6 Conclusion

In this work, we tried to test the accuracy of the Variational Monte Carlo method with gradient descent optimization for the 2-electrons harmonium quantum system and compare the results with exact calculation. Our calculations make use of a two-parameter Gaussian trial wave function and the results showed that the method converges well and yields good results. The accuracy can be improved by choosing a better trial function with more parameters.

References

[1] N. R. Kestner; O. Sinanoglu Phys. Rev. 128 (6): 2687-2692 (1962)
[2] S. Kais & al, J. Chem. Phys. 91 (12): 7791 (1989).
[3] S. Kais & al, J. Chem. Phys. 99 (1): 417-425.(1993).
[4] M. Taut, Phys. Rev. A. 48 (5): 3561-3566 (1993)
[5] J. Cioslowski & K. Pernal, The Journal of Chemical Physics 113, 8434(2000)
[6] J. Cioslowski, Teoretica Chimica Acta 137 (12), 173 (2018)

J. Phys. &Chem. Res. 4, Issue 1, June (2025) 43–48

Journal of Physical & Chemical Research

Journal homepage:https://ojs.univ-bba.dz

Formulation d'encre industrielle à base d'eau comme solution écologique

Meriem Hamla[1, 2 *], Anfal Samar Zedam[1], Khalil Ghersallah[1], Amamra Samra[1,3], Hamza Behloul[1],

[1]Département Sciences de la Matière, Faculté des sciences et de la Technologie, Université de Mohamed El-Bachir El-Ibrahimi , 34000 - Bordj Bou Arréridj, ALGERIE

[2]Laboratoire d'Energétique et d'Electrochimie du Solide (LEES), Département de Génie des procédés, Faculté de Technologie, Université Sétif1, 19000-Sétif, ALGERIE.

[3]Laboratoire d'électrochimie des matériaux moléculaires et complexes (LEMMC). Faculté de technologie. Université Ferhat Abbas Sétif-1, 19000, Algérie.

** Corresponding author: Tel./Fax: +0-000-000-0000 ; E-mail address: meriem.hamla@univ-bba.dz*

Historique de l'article

Received December 8, 2024

Accepted for publication January 12, 2025

Résumé

Les encres à base d'eau représentent une alternative écologique et performante pour une qualité d'impression optimale. Les encres aqueuses offrent des performances de 20 à 30% supérieures à celles des encres à base de solvants, avec l'avantage d'obtenir une viscosité stable, réduisant ainsi la nécessité d'ajouter des solvants pendant l'impression. Cette étude propose une formulation d'encre à base d'eau pour l'imprimerie industrielle, offrir une alternative plus respectueuse de l'environnement diminuer les émissions de composés organiques volatils (COV) et les dangers sur la santé liée à l'utilisation de solvants chimiques en utilisant de l'eau comme base.

La composition chimique est variée entre l'eau distillée avec un pourcentage (60-70 %), et d'autres additifs comme (l'antimousse, accélérateur ou retardateur de séchage et les pigments selon la couleur désirée. La nouvelle formulation assure une amélioration de qualité et diminuer les impacts environnementaux.

Mots-clés : Encre à base d'eau, solution écologique, imprimerie industrielle, viscosité.

1. Introduction

Les encres aqueuses sont une alternative plus durable et plus respectueuse de l'environnement et plus sécurisée à celles des encres à base de solvants [1].

L'encre à base d'eau est un type d'encre composée principalement par l'eau, de résines spécifiques qui confèrent à l'encre des propriétés de brillance et de résistance chimique, de pigment et d'autres additifs [2]. Elle est utilisée sur une large gamme de supports d'impression sans causer de dommages [3], en raison de sa viscosité stable et son caractère écologique. Aussi c'est un choix polyvalent pour différentes applications d'impression, à cause des pigments utilisés qui peuvent produire une large gamme de couleurs.

L'encre à base d'eau présente un meilleur choix pour l'industrie de l'impression. L'un de ses principaux avantages est son caractère écologique, l'eau est le principal solvant qui lui rend moins nocive pour l'environnement par rapport à d'autres types d'encres à base de solvants chimiques. Ce travail fournir une étude complète sur sa composition, ces avantages et ces techniques d'impression utilisés lors de son fabrication.

2. Méthodologie

Cette étude a pour objectif d'évaluer la faisabilité et les performances d'une encre écologique à base d'eau, élaborée à partir de matériaux naturels et durables, dans une optique de réduction de l'impact environnemental. La formulation repose sur l'utilisation de pigments organiques et de liants biodégradables, intégrés via des procédés respectueux de l'environnement. Cette approche vise à offrir une alternative plus durable aux encres traditionnelles à base de solvants, tout en garantissant des performances comparables en termes de qualité d'impression, de stabilité, et de durabilité sur divers supports.

Pour concevoir cette encre à base d'eau distillée, différents composants ont été soigneusement sélectionnés et combinés : un tensioactif pour ajuster la viscosité, un colorant (ou teinture) servant d'agent colorant, un tampon pour réguler le pH, et un agent antimousse utilisé si nécessaire pour éviter la formation de bulles. La viscosité a été mesurée à l'aide d'un viscosimètre, tandis que la tension superficielle a été déterminée avec un tensiomètre, permettant d'optimiser les propriétés physiques de l'encre. Les ajustements nécessaires ont été effectués en fonction des résultats obtenus.

Le processus de production s'est déroulé en plusieurs étapes. Tout d'abord, le colorant a été dissous dans l'eau distillée, suivi de l'ajout du tensioactif. Le mélange a été soumis à une homogénéisation mécanique à une vitesse de 500 tr/min pendant 15 minutes afin d'assurer une distribution uniforme des composants. Une fois le mélange homogène, le pH a été mesuré et ajusté à une valeur légèrement basique (adaptée aux exigences de l'impression) en ajoutant un tampon. Pour éviter toute formation de mousse indésirable, une goutte d'agent antimousse a été intégrée à la formulation finale. Après la préparation, la stabilité physique et chimique de l'encre a été examinée visuellement sur une période de 72 heures, afin de s'assurer de l'absence de séparation de phases, de précipitation ou d'altération des propriétés.

2.1.Matériaux et équipements

Les tests de caractérisation des encres ont été réalisés à l'aide des équipements suivants : une balance de précision pour peser les différents composants avec exactitude, un pH-mètre pour mesurer et ajuster le pH des formulations, un pycnomètre pour déterminer la densité avec précision. La viscosité des encres a été mesurée à l'aide d'une coupe de viscosité Ford pour des mesures rapides et d'un viscosimètre à chute de bille type C pour des valeurs plus précises.

Un densimètre portable a été utilisé pour des contrôles instantanés de densité, et un Anilox Handproofer a servi à simuler le processus d'impression, permettant une évaluation de la couverture et de la qualité d'application de l'encre sur différents supports. Ces équipements, utilisés de manière complémentaire, ont permis d'obtenir des données fiables sur les propriétés physico-chimiques des encres testées.

Figure 1. Une coupe de viscosité

Figure 2. Pycnomètre

Ford

Figure 3. Un densimètre portable

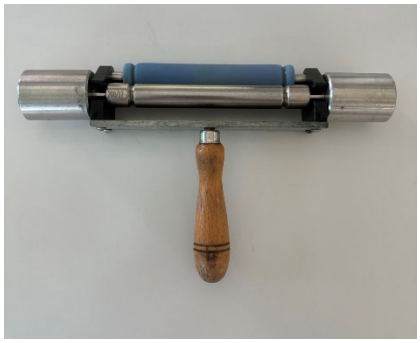

Figure 4. Anilox Handproofer

Figure 5. Viscosimètre à chute de bille type C

3. Résultats

Les propriétés physico-chimiques des encres formulées pour différents supports (papier extra et carton) ont été évaluées, et les résultats obtenus (tableau 1), montrent une adaptation satisfaisante aux exigences spécifiques de chaque type de surface. Les paramètres mesurés incluent le pH, la densité et la viscosité, chacun étant essentiel pour garantir l'efficacité et la compatibilité des encres avec les supports.

Tableau 1 : Les propriétés physico-chimiques des encres formulées pour différents supports (papier extra et carton)

Produits	pH	Intervalle pH	Densité (g/cm³)	Intervalle Densité (g/cm³)	Viscosité (cP)	Intervalle Viscosité (cP)
papier extra	8,68	7 à 9	1,28	1,0 à 1,3	107,4	10 à 500
carton	8,41	7 à 9	1,27	1,0 à 1,5	113,28	12 à 500

4. Discussion

À la suite des expériences d'impression avec des encres ayant des valeurs différentes, Le pH des encres varie entre 8,41-8,68 pour le carton et le papier extra respectivement. Ces valeurs se situent principalement dans les intervalles ciblés, confirmant la stabilité chimique des formulations.

Les densités mesurées pour les encres sont 1,28 g/cm³ pour le papier extra et 1,27 g/cm³ pour le carton, toutes restant dans les plages ciblées. Les différences observées (notamment la densité plus élevée pour les encres de papier extra et carton) peuvent être attribuées à une concentration plus importante de composants tels que les colorants et les additifs, nécessaires pour optimiser la couverture et l'adhérence, en particulier sur des supports plus poreux ou épais.

Les viscosités mesurées varient significativement : 107,4 cP pour le papier extra, et 113,28 cP pour le carton. Cette variation est logique étant donné les propriétés des supports. L'encre pour papier extra et carton présente des viscosités élevées, ce qui est adapté pour éviter des problèmes d'absorption excessive et pour garantir une bonne couverture et stabilité de l'encre.

5. Conclusion

Les encres à base d'eau offrent une alternative plus écologique et économique que les encres à base de solvant, tout en maintenant une qualité d'impression optimale. Elles répondent ainsi aux exigences environnementales et de performance de l'industrie de l'impression. L'absence de solvants dans les encres à base d'eau diminue les coûts liés à leur gestion et leur stockage. De plus, le processus d'impression peut être plus simple et moins coûteux à long terme.

Elles peuvent être utilisées sur une grande variété de supports, ce qui les rend adaptées à de nombreuses applications industrielles, tout en maintenant une excellente adhérence et résistance. Avec une viscosité stable, ce qui réduit la nécessité d'ajuster constamment les paramètres d'impression.

References

[1] B. Jarrehult, R.G. Horacek, M.L. Lindquist, « Deinking of Wastepaper Containing Flexographic Inks », Pulping Conference (Seattle) Proceedings, Book 1, (octobre 1989) 391-405.

[2] B. Chabot, C. Daneault , M. Lapointe, L. Marchildon, "Newsprint Water-Based Inks and Flotation Deinking", Progress in Paper Recycling, (août 1993).

[3] F. Mathieu, « optimisation des paramètres d'impression pour l'électronique imprimée sur support souples », Institut National Polytechnique de Grenoble - NPG, 2007.

J. Phys. &Chem. Res. 4, Issue 1, June (2025) 49–64

Journal of Physical & Chemical Research

Journal homepage:https://ojs.univ-bba.dz

Etude in-silco via docking moléculaire de l'inhibition de la xanthine oxydoréductase et du NADPH oxydase par la zéaxanthine et l'astaxanthine

Amamra Samra[1,2*], Kaabi Ilhem[2*], Hamla Meriem[1, 3], Chafai Nadjib[2]

[1] Département des sciences de la matière, Faculté des sciences et de la technologie, Université Mohamed El-Bachir El-Ibrahimi de Bordj Bou Arréridj.
[2]Laboratoire d'électrochimie des matériaux moléculaires et complexes (LEMMC). Faculté de technologie. Université Ferhat Abbas Sétif-1, 19000, Algérie.
[3]Laboratoire d'énergetique et électrochimie du solide (LEES), Université Ferhat Abbas- Sétif-1- 19000, Algerie.
** Auteurs correspondants : tél 06 98 01 07 78 ; E-mail : kaabi_ilh@yahoo.fr & samra.amamra@univ-bba.dz*

Article history
Received December 2, 2024
Accepted for publication January 7, 2025

Résumé

La recherche en chimie et biologie ne peut actuellement se passer des outils informatiques pour traiter les données produites et optimiser ses avancées. L'un de ces outils est la modélisation moléculaire et plus précisément l'amarrage moléculaire (plus souvent connu sous le terme "docking"). Le docking moléculaire est principalement utilisé pour prédire et reproduire les complexes ''protéines-ligands'' en reconnaissant les différents types d'interactions.

Dans ce travail. Nous avons utilisé l'approche du docking moléculaire pour étudier et vérifier l'activité antioxydante de deux molécules « astaxanthine et zéaxanthine » en utilisant le logiciel de docking iGEMDOCK. Il consiste à vérifier l'interaction entre les deux enzymes : NADPH oxydase et la xanthine oxydase qui sont impliquées dans la production endogène des radicaux libres avec deux antioxydants puissants : la zéaxanthine et l'astaxanthine. Les résultats de notre approche in-silico ont prouvé que l'astaxanthine et la zéaxanthine ont une bonne affinité avec les deux enzymes.

Mots-clés : enzymes, inhibiteurs, docking moléculaire, score, NADPH, xanthine oxydase, zéaxanthine, astaxanthine.

1. Introduction

Le développement, au cours de ses dernières années, des moyens informatiques (ordinateurs puissants, logiciels .... etc.) a permis à la chimie de s'enrichir d'outils spécialement dédiés à la représentation des molécules et au calcul de différents paramètres. La conception in-silico a contribué à réduire les coûts et les délais associés à la découverte de médicaments en orientant plus rapidement la recherche expérimentale vers les composés optimaux [1,2].

La modélisation moléculaire est une approche scientifique multidisciplinaire: elle utilise des lois de la chimie, de la physique et de la biologie dans des programmes informatiques spécifiques afin de trouver la structure et les propriétés de composés chimiques et biochimiques (protéines, acides nucléiques, complexes moléculaires, solides, cristaux etc.). Elle permet d'étudier des systèmes complexes et de représenter leur comportement avec leur environnement [3]. La modélisation moléculaire s'est développée grâce à l'évolution de l'informatique qui a permis d'intégrer les concepts de chimie théorique dans les algorithmes et de développer des machines capables d'exécuter les lourds calculs demandés et de stocker les données générées [4,5]. Ces applications permettent l'étude au niveau atomique d'interactions entre deux entités moléculaires. Elles visent la prédiction de l'agencement le plus probable d'un ligand au sein de son récepteur en cherchant des orientations dans l'espace et des conformations qui favorisent la formation du complexe ligand-récepteur le plus stable [6]. Dans ce cadre, des techniques telles que le docking moléculaire et le criblage virtuel ont apporté un complément précieux au processus expérimental coûteux en temps et en argent.

Dans ce contexte l'objectif de notre travail est l'étude in silico le mécanisme d'inhibition des enzymes NADPH oxydase et la xanthine oxydoreductase par deux antioxydants la zéaxanthine et l'astaxanthine. En utilisant les logiciels iGEMDOCK et Discovery studio 2016. Cette étude comprend la connaissance:

- Du site actif de la protéine dans lequel chaque ligand est placé.
- Des distances des interactions formées entre les ligands et les acides aminés de la protéine.
- Des types des interactions entre les ligands et les enzymes et leurs énergies.

2. Docking moléculaire

2.1. Préparation des enzymes

La structure cristalline des enzymes (NADPH Oxydase et la xanthine oxydoréductase) a été téléchargée sous l'extension format **PDB** à partir de la base de données **P**rotéine **D**ata **B**ank (www.rcsb.org/pdb) en utilisant les codes d'accès (50OX, 3B9J) respectivement, les structures

(3D) tridimensionnelles des enzymes trouvés sont montrées dans la figure suivante :

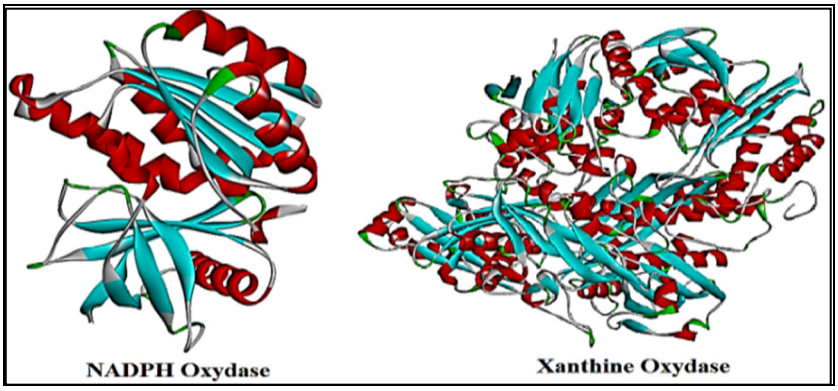

Figure 1. La structure tridimensionnelle des enzymes : NADPH Oxydase et xanthine oxydoréductase

.*2.2. Préparation des ligands*

Les ligands utilisés dans ce travail (l'astaxanthine et la zéaxanthine) sont des dérives du β-caroténe. La figure.2 représente les structures tridimensionnelles optimisées des ligands étudiés en format (PDB).

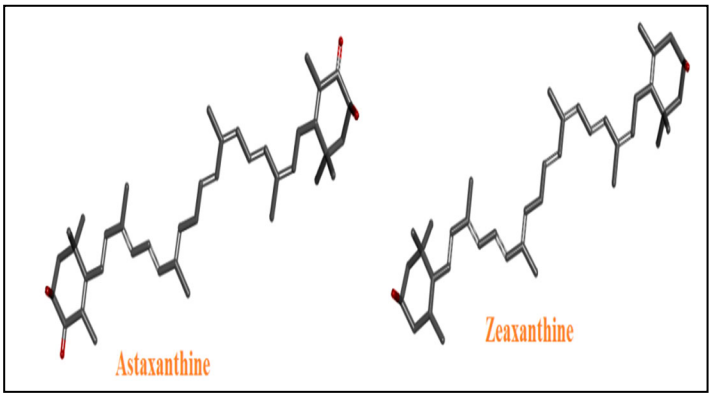

Figure 2. Structure tridimensionnelle des ligands.

2.3. Etude de l'interaction entre les ligands et les enzymes

2.3.1. NADPH oxidase avec l'astaxanthine et la zéaxanthine

La figure suivante représent les meilleures poses d'interactions des complexes NADPH-oxydase-astaxanthine et NADPH-oxydase-zéaxanthine.

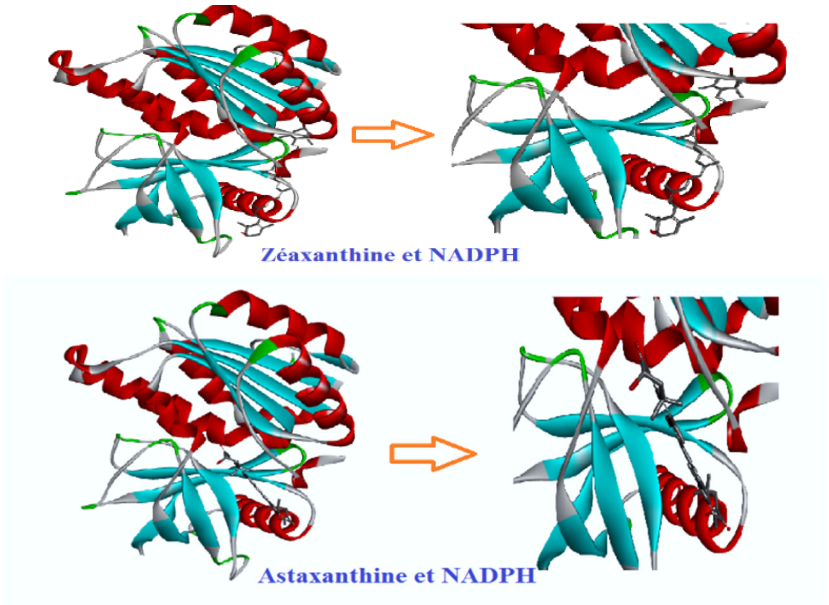

Figure 3. Illustration de meilleures poses (amarrées) d'interactions des ligands étudiés avec le NADPH oxydase.

a- Astaxanthine avec le NADPH oxydase

La **figure 4** représente le diagramme d'interactions en 2D de l'astaxanthine avec le NADPH oxydase.

L'examen de cette figure montre les informations suivantes :

- Des forces de VDW avec les acides aminés : TRP A483, THR A484, ASN A692, GLU A691.
- Une liaison Pi-sigma avec l'acide aminé : TRP A695.
- Des liaisons alkyle et Pi-alkyle avec les aminoacides : HIS A459, PHE A461, VAL A480, PRO A460, PRO A694, PHE A693, TRP A695, ARG A689, PRO A521, LYS A690.

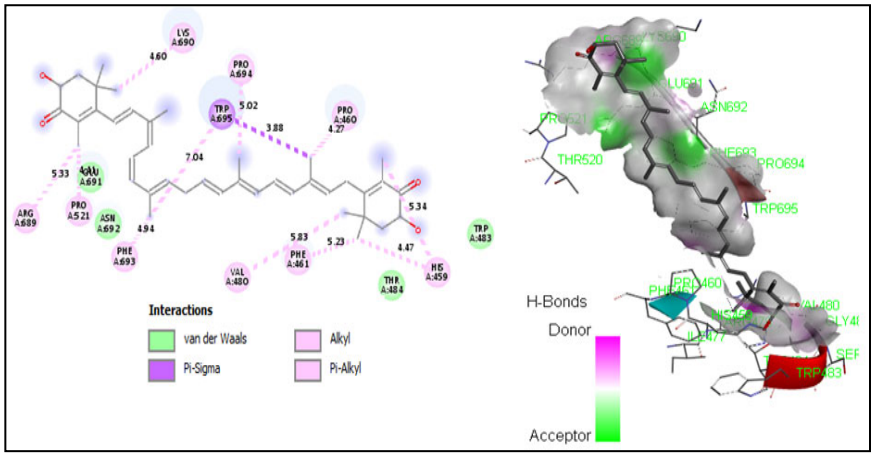

Figure 4. Diagramme d'interactions en 2D et 3D entre l'astaxanthine et le NADPH oxydase.

L'analyse visuelle de la **figure.4** montre que l'astaxanthine forme 16 liaisons avec le NADPH oxydase:

- **04 liaisons** de type **VDW** avec: TRP A483, TRH A484, ASN A692, GLU A691.
- **11 liaisons** (**alkyle et Pi-alkyle**) se forment entre les radicaux méthyles (**-CH_3**) et les aminoacides du site actif:

-CH_3 du **C2** du cycle (6S)-6-hydroxy-3]-2,4,4-trimethyl-1-cyclohex-2-enone du ligand et le résidu HIS A459 du site actif de l'enzyme avec une langueur de liaison de 5.34A°.

-CH_3 du **C4** du cycle (6S)-6-hydroxy-3]-2,4,4-trimethyl-1-cyclohex-2-enone du ligand et les résidus HIS A459, PHE A461 et VAL A480 du site acif de l'enzyme qui ont des distances de 4.47A°, 5.23 A° et 5.83A° respectivement.

-CH_3 du **C3** du radical 3,7,12,16-tetramethyloctadeca-1,3,5,7,9,11,13,15,17-nonaenyl du ligand et le résidu PRO A460 du site actif de l'enzyme avec une distance de 4.27A°.

-CH_3 du **C7** du radical 3,7,12,16-tetramethyloctadeca-1,3,5,7,9,11,13,15,17-nonaenyl du ligand et le résidu PRO A694 du site actif de l'enzyme avec une langueur de liaison de 5.02A°.

-CH_3 du **C12** du radical 3,7,12,16-tetramethyloctadeca-1,3,5,7,9,11,13,15,17-nonaenyl du ligand et les résidus PHE A693 et TRP A695 du site actif de l'enzyme avec des distances de 4.94A° et 7.04A°

respectivement.

-CH_3 du **C2** du radical -4-hydroxy-2,6,6-trimethyl-3-oxo-1-cyclohexenyl du ligand et les résidus ARG A689 et PRO A521 du site actif de l'enzyme avec des langueurs des liaisons de 5.33A° et 4.41A° respectivement.

-CH_3 du **C6** du radical -4-hydroxy-2, 6,6-trimethyl-3-oxo-1-cyclohexenyl du ligand et le résidu LYS A690 du site actif de l'enzyme avec une langueur de liaison de 4.60A°.

- Une **liaison Pi-sigma** se forme entre **-CH_3** du **C3** du radical 3, 7, 12,16-tetramethyloctadeca-1,3, 5, 7, 9, 11, 13, 15,17-nonaenyl du ligand et le résidu TRP A695 du site acif de l'enzyme avec une distance de 3.88A°.

Comme le montre la **figure.4** (la visualisation des interactions en 3D), les zones vertes représentent les régions accepteuses, tandis que les zones roses représentent les régions donneuses. Il a été révélé que l'interaction du complexe inhibiteur-récepteur calculée théoriquement a donné des résultats satisfaites, pour l'astaxanthine, on trouve que les fonctions cétone et alcool possède une zone rose et les radicaux méthyles possèdent des zones vertes.

b- Zéaxanthine avec le NADPH oxydase

La **figure 5** représente le diagramme d'interactions en 2D de la zéaxanthine avec le NADPH oxydase, l'examen de cette figure montre :

- Des liaisons de VDW avec les acides aminés : SER A425, GLY A537, GLU A574, PHE A461, PHE A447, TRP A458, GLU A574.
- Des liaisons d'hydrogène avec les aminoacides : ARG A573, ASN A572.
- Une liaison électrostatique avec l'acide aminé : TRP A580.
- Des liaisons de type alkyle et Pi-alkyle avec les aminoacides : ALA A577, ILE A538, ARG A573, LEU A696, TRP A695, VAL A480, ARG A478, PRO A460, HIS A459.

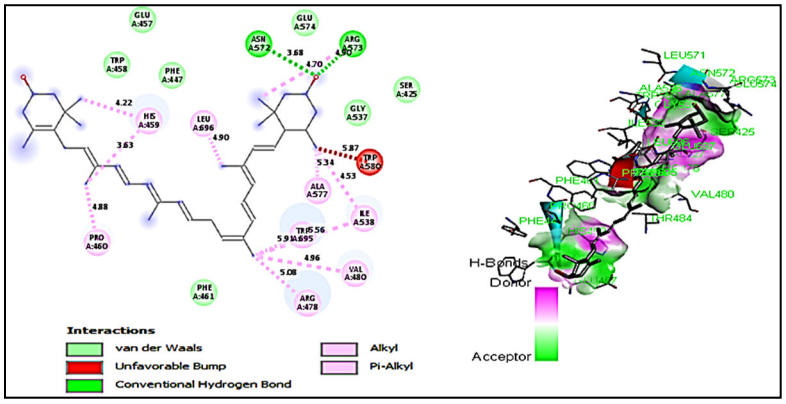

Figure 5. Diagramme d'interactions en 2D et 3D de la zéaxanthine avec le NADPH oxydase.

L'analyse visuelle de la **figure.5** montre que la zéaxanthine forme globalement 21 liaisons avec le récepteur NADPH oxydase:

- Une **interaction électrostatique** entre le groupement (**-CH_3**) du **C3** du cycle 3,5,5-triméthyl-cyclohex-3-én-1-ol et le résidu TRP A580 du site actif de l'enzyme avec une distance de 5.87Å.
- **7** interactions de type de **VDW** avec les résidus: SER A425, GLY A537, GLU A574, PHE A461, PHE A447, TRP A458, GLU A574.
- **12** liaisons de type **Pi-alkyle** et **alkyle** se forment entre les groupements (**-CH_3**) et les résidus aminoacides de l'enzyme:

-CH_3 du **C3** du cycle 3,5,5-triméthyl-cyclohex-3-én-1-ol du ligand et les résidus ALA A577 et ILE A538 avec des distances de 5.34A° et 4.53A° respectivement.

-CH_3 du **C5** du cycle 3,5,5-triméthyl-cyclohex-3-én-1-ol du ligand et le résidu ARG A573 avec une distance de 4.70A°.

-CH_3 du **C3** du radical -3,7,12,16-tétraméthyloctadéca-1,3,5,7,9,11,13,15,17-nonaényl du ligand et le résidu LEU A696 du site actif de l'enzyme avec une langueur de liaison de 4.90A°.

-CH_3 du **C7** du radical -3,7,12,16-tétraméthyloctadéca-1,3,5,7,9,11,13,15,17-nonaényl du ligand et les résidus TRP A695, VAL A480, ARG A478 et ILE A538, du site actif de l'enzyme avec des langueurs des liaisons de 5.91A°, 4.96A°, 5.08A° et 5.56A° respectivement.

-CH_3 du **C16** du radical -3,7,12,16-tétraméthyloctadéca-1,3,5,7,9,11,13,15,17-nonaényl du ligand et les résidus PRO A460 et HIS A459 du site actif de l'enzyme avec des langueurs des liaisons de 4.88A° et 3.63A° respectivement.

-CH_3 du **C6** du radical -18-(4-hydroxy-2,6,6-triméthyl-1-cyclohexényl du ligand et le résidu HIS A459 du site actif de l'enzyme avec une langueur de liaison de 4.22A°.

- **2** liaisons **d'hydrogènes** entre l'**O** du **C1** du cycle 3,5,5-triméthyl-cyclohex-3-én-1-ol du ligand et les résidus ARG A573 et ASN A572 avec des distances de 4.90A° et 3.68A° respectivement.

D'après le diagramme 3D, on observe que:

- Les groupes -OH des cycles sont entourées par des zones en couleur rose ceci montre leurs povoirs donneurs.
- Les groupements alkyles sont entourés par des zones vertes ce qui indique leurs pouvoirs accepteurs.

2.3.2. Les énergies des liaisons entres les ligands et le NADPPH oxydase

La distribution d'énergie des inhibiteurs étudiés entre les forces de van der Waals, la liaison hydrogène et les interactions électrostatiques sont présentée dans le **tableau.1**.

Tableau 1: Résultats de score du récepteur NAPDH oxydase avec les ligands.

NADPH oxydase			
	EvdW Kcal/mol	**E H-bond Kcal/mol**	**E IEl Kcal/mol**
Ligand 01(zéaxanthine)	-94.97	-6	0
Ligand 02(astaxanthine)	-96.91	-4.22	0
Energie totale Kcal/mol			
Ligand 01(zéaxanthine)	-100.97		
Ligand 02(astaxanthine)	-101.13		

EvdW : energie de van der Waals*,* ***EH-bond*** *: energie des liaisons d'dydrogène****, EIEl****: enegrie d'interaction électristatique.*

Les calculs d'amarrage (**figure 6** et **tableau 1**) ont conduit aux résultats suivants : le ligand astaxanthine possède les interactions de van der Waals les plus fortes (EvdW = -96.91 kcal/mol), tandis que la zéaxanthine a montré l'énergie de liaison hydrogène la plus élevée (EH-

bond = -6 kcal/mol). Ainsi l'astaxanthine présente la valeur la plus basse d'énergie de la liaison dans les interactions moléculaires (-101.13 kcal/mol) avec le NADPH oxydase ce qui indique que cet inhibiteur a une **meilleure affinité** et **réactivité** *vis-à-vis* de cet enzyme plus que de la zéaxanthine (-100.97 Kcal/mol).

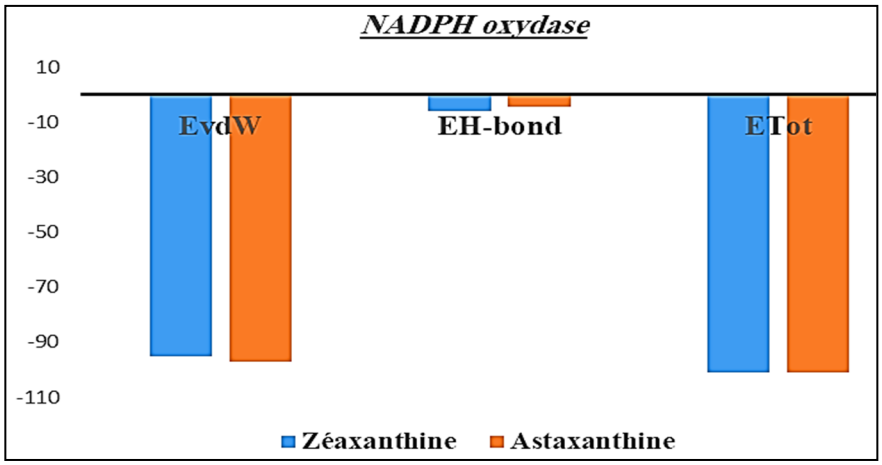

Figure 6. Histogramme représente les énergies d'interaction du récepteur NADPH oxydase avec les ligands.

2.3.3. La xanthine oxydoréductase avec l'astaxanthine et la zéaxanthine

La figure suivante représent les meilleures poses d'interactions des complexes xanthines oxydoréductase-astaxanthine et xanthine oxydoréductase-zéaxanthine:

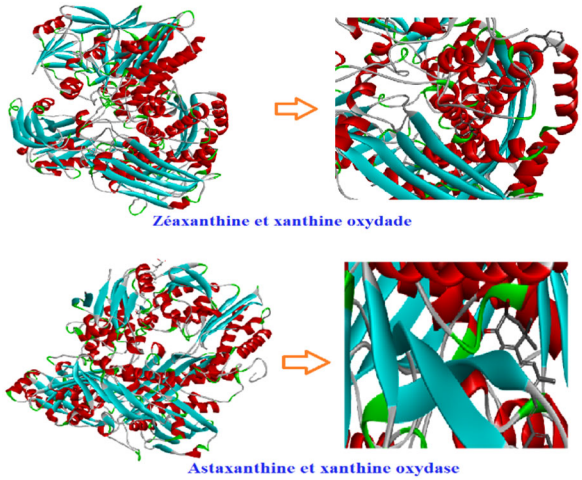

Figure 7. Illustration de meilleures poses d'interactions des ligands étudiés avec la xanthine oxydoréductase.

c- Astaxanthine avec la xanthine oxydoréductase

D'après la **figure 8**, on remarque que l'astaxanthine se lie avec la xanthine oxydoréductase, en formant les interactions suivantes :

- Des interactions de type de **VDW** avec les acides aminés: GLU B291, ASN B288, GLN A62, THR B311, SER B307, SER B344, SER B306, PHE A68, SER A123, THR A126, ALA A142, ASN A130.
- Une liaison électrostatique avec l'acide aminé: ALA B289.
- Des liaions de type alkyle avec les acides aminés: LEU A61, LYS B310, ILE A66, LYS AB340, LEU A127.
- Une liaison d'hydrogène avec le résidu SER A69.

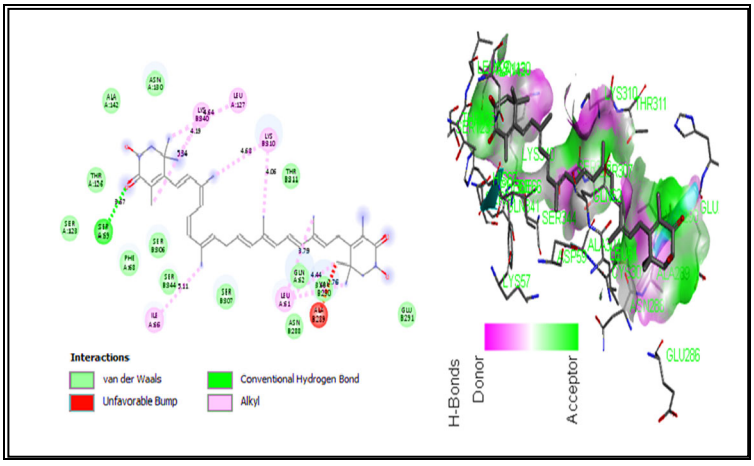

Figure 8. Diagramme d'interactions en 2D et 3D de l'astaxanthine avec la xanthine oxydoréductase.

L'analyse visuelle de la **figure.8** montre que l'astaxanthine forme 23 liaisons de différents types avec la xanthine oxydoréductase :

- **12 liaisons** de type **VDW** avec des résidus : GLU B291, ASN B288, GLN A62, THR B311, SER B307, SER B344, SER B306, PHE A68, SER A123, THR A126, ALA A142, ASN A130.
- **09 liaisons alkyles** se forment entre les groupements méthyl (**-CH_3**) et les aminoacides du site actif :

-CH_3 du **C4** du cycle (6S)-6-hydroxy-3]-2,4,4-trimethyl-1-cyclohex-2-enone du ligand forme deux liaisons avec le résidu LEU A61 de site actif de l'enzyme avec des langueurs des liaisons de 4.44A° et 2.76A°.

-CH_3 du **C3** du radical -3,7,12,16-tetramethyloctadeca-1,3,5,7,9,11,13,15,17-nonaenyl du ligand et le résidu LEU A61 de site actif

de l'enzyme avec une distance de 3.79A°.

-CH_3 du **C7** du radical -3,7,12,16-tetramethyloctadeca-1,3,5,7,9,11,13,15,17-nonaenyl du ligand et le résidu LYS B310 du site actif de l'enzyme avec une langueur de liaison de 4.06A°.

-CH_3 du **C12** du radical -3,7,12,16-tetramethyloctadeca-1,3,5,7,9,11,13,15,17-nonaenyl du ligand et le résidu ILE A66 du site actif de l'enzyme avec une distance de 5.11A°.

-CH_3 du **C16** du radical -3,7,12,16-tetramethyloctadeca-1,3,5,7,9,11,13,15,17-nonaenyl du ligand et le résidu LYS B310 du site actif de l'enzyme avec une langueur de liaison de 4.68A°.

-CH_3 du **C2** du radical -4-hydroxy-2,6,6-trimethyl-3-oxo-1-cyclohexenyl du ligand et le résidu LYS B340 de site actif de l'enzyme avec une langueur de liaison de 5.34A°.

-CH_3 du **C6** du radical -4-hydroxy-2,6,6-trimethyl-3-oxo-1-cyclohexenyl du ligand et les résidus LEU A127 et LYS B340 de site actif de l'enzyme avec des langueurs des liaisons de 4.64A° et 4.19A° respectivement.

- Des **interactions électrostatiques** se forment entre le groupe **–CH_3 du C4** du cycle (6S)-6-hydroxy-3]-2,4,4-trimethyl-1-cyclohex-2-enone du ligand et le résidu ALA B289 de l'enzyme avec une distance de 2.76A°.
- Une **liaison d'hydrogène** entre le groupement **cétone** du radical -4-hydroxy-2,6,6-trimethyl-3-oxo-1-cyclohexenyl du ligand et le résidu SER A69 de site actif de l'enzyme avec une langueur de liaison de 3.67A°.

Selon la **figure 8** (la visualisation des interactions en 3D), on observe que :

- L'atome de l'oxygèn de la fonction cétone entourée par une zone de couleur verte, ce qui indique leurs effets accepteurs et crée une liaison hydrogène avec SER A69.
- Les groupes méthyles sont entourés par une zone de couleur rose, ce qui montre donc leurs pouvoirs donneurs.
- L'atome d'oxygène du groupe (OH) du cycle agit comme un donneur.

d- Zéaxanthine avec la xanthine oxydoréductase

D'après la **figure.9**, on remarque que la zéaxanthine se lie avec la xanthine oxydoréductase en formant :

- Une liaison d'hydrogène avec l'acide aminé: SER C731.

- Des interactions de VDW avec les acides aminés: VAL C730, PHE C1294, GLU C1292, ASN C1289, THR C1286, ARG C1282, ASN C1287, ASN C1288, TRP C1328.
- Des liaisons alkyles avec les acides aminés : LEU C1293, CYS C1325, PRO C1327.

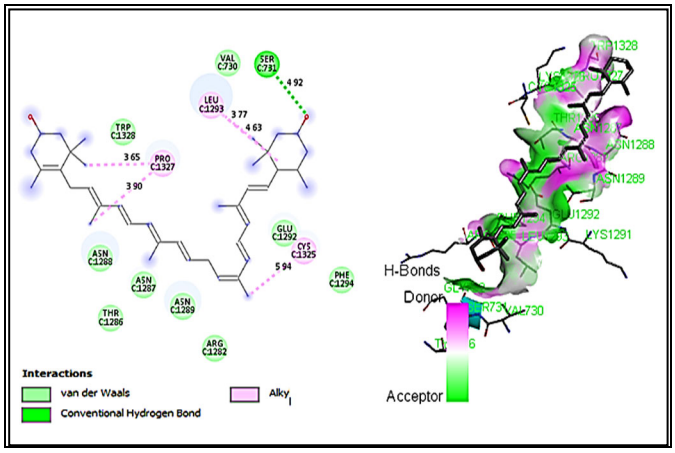

Figure 9. Diagramme d'interactions en 2D et 3D de la zéaxanthine avec la xanthine oxydoréductase.

L'analyse visuelle de la **figure.9** montre que le zéaxanthine se forme 15 liaisons avec le récepteur xanthine oxydoréductase :

- **9 interactions VDW** avec les aminoacides : VAL C730, PHE C1294, GLU C1292, ASN C1289, THR C1286, ARG C1282, ASN C1287, ASN C1288, TRP C1328.
- **Une liaison d'hydrogène** entre le groupement hydroxyde du cycle 3,5,5-triméthyl-cyclohex-3-én-1-ol du ligand et le résidu SER C731 avec une distance de. 4.92A°.
- **5 liaisons alkyles** des groupements **-CH_3** réparties comme suit :

-CH_3 du **C3** du cycle 3,5,5-triméthyl-cyclohex-3-én-1-ol du ligand et le résidu LEU C1293 avec une distance de 3.77 A°.

-CH_3 du **C5** du cycle 3,5,5-triméthyl-cyclohex-3-én-1-ol du ligand et le résidu LEU C1293 avec une distance de 4.63A°.

-CH_3 du **C7** du radical -3,7,12,16-tétraméthyloctadéca-1,3,5,7,9,11,13,15,17-nonaényl du ligand et le résidu CYS C1325 du site actif de l'enzyme avec une langueur de liaison de 5.94A°.

-CH_3 du **C16** du radical -3,7,12,16-tétraméthyloctadéca-1,3,5,7,9,11,13,15,17-nonaényl du ligand et le résidu PRO C1327 du site actif de l'enzyme avec une langueur de liaison de 3.90A°.

-CH_3 du **C6** du radical -18-(4-hydroxy-2,6,6-triméthyl-1-cyclohexényl du ligand et le résidu PRO C1327 du site actif de l'enzyme avec une langueur de liaison de 3.65A°.

Selon la figure.9 (la visualisation tridimensionnelle des interactions en 3D), on observe que :

- ❖ Le groupe (OH) du cycle agit comme un donneur.
- ❖ Les groupements méthyles sont entourés par des régions de couleur verte, ce qui représente donc des sites accepteurs.

2.3.4. Les énergies des liaisons entres les ligands et la xanthine oxydoréductase

La distribution de l'énergie sur les différents types d'interaction (les liaisons
d'hydrogène, les forces de Van Der Waals et les interactions électrostatiques) des complexes astaxanthine-xanthine oxydoréductase et zéaxanthine-xanthine oxydoréductase sont reportés dans le **tableau 2**.

Tableau 2. Résultats de score du récepteur de la xanthine oxydase avec les ligands.

Xanthine oxydoréductase			
	EvdW (Kcal/mol)	**EH-bond (Kcal/mol)**	**EIEl (Kcal/mol)**
Ligand 01(zéaxanthine)	-82.13	-2.50	0
Ligand 02(astaxanthine)	-103.79	-6.00	0
Energie totale (Kcal/mol)			
Ligand 01(zéaxanthine)	-84.63		
Ligand 02(astaxanthine)	-109.79		

EvdW : energie de van der Waals, ***EH-bond*** *: energie des liaisons d'dydrogène,* ***EIEl****: enegrie d'interaction électristatique.*

Comparant les valeurs obtenues de l'énergie de liaison des ligands étudiés (**figure 10**), nous observons que l'astaxanthine présente la valeur la plus basse d'énergie dans les intéractions avec la xanthine oxydase (-109.79 Kcal/mol), ce qui indique leur **meilleure affinité** et leur **meilleure stabilité** *vis-à-vis* de ce récepteur, que ce formé pour la zéaxanthine (-84.63 Kcal/mol). Et par conséquence l'astaxanthine a **une meilleure efficacité** et une **bonne**

activité inhibitrice *vis-à-vis* de la xanthine oxydase.

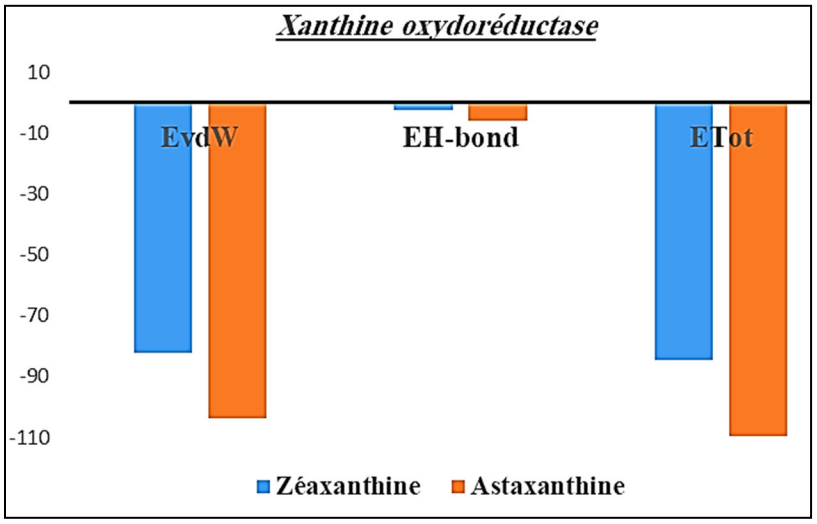

Figure 10. Histogramme représente les énergies d'interaction du récepteur xanthine oxydase avec les ligands.

3. résultats et discussion

Les enzymes sont des molécules bien plus grandes que leurs substrats. Leur taille varie de 62 résidus à plus de 2 000 résidus. Seule une toute petite partie de l'enzyme est directement impliquée dans la catalyse, ce qu'on appelle le site catalytique. Ce dernier est situé à proximité d'un ou plusieurs sites de liaison, au niveau desquels les substrats sont liés et orientés afin de permettre la catalyse de la réaction chimique. Le site catalytique et les sites de liaison forment le site actif de l'enzyme. Le reste de la protéine sert à maintenir la configuration du site actif et à y générer les conditions optimales pour le déroulement de la réaction.

Le site actif est constitué d'un petit nombre d'acides aminés qui le plus souvent ne sont pas contigus dans l'enchaînement de la chaîne polypeptidique. Ces acides aminés sont caractérisés par une chaîne latérale dont à la fois la nature chimique (groupement ionisable) et la structure (encombrement stérique) sont spécifiquement adaptés à la reconnaissance du substrat.

Les enzymes doivent tout d'abord se lier à leurs substrats avant de pouvoir catalyser toute réaction chimique. Les enzymes sont plus ou moins spécifiques en ce qui concerne à la fois les substrats auxquels elles peuvent se lier et les réactions qu'elles sont susceptibles de catalyser. Cette spécificité résulte de la configuration de leurs sites de liaison, qui sont des

poches présentant une complémentarité de forme ainsi que de distribution spatiale des charges électriques et des propriétés hydrophile/hydrophobe par rapport à celles du substrat. Les enzymes peuvent ainsi faire la différence entre des molécules très semblables, ce qui assure leur chimiosélectivité, leur régiosélectivité et leur stéréospécificité **[7,8].**

A partir les résultats présentés ci-dessus, on observe que lorsque le ligand (astaxanthine /zéaxanthine) est attaché avec leur site actif il forme des liaisons de type: les liaisons d'hydrogènes, les liaisons de van der Waals, les intéractions éléctrostatiques…). Mais nous avons remarqué que les interactions de van der Waals ont les valeurs de l'énergie la plus négative, ce qui montre que ce type d'interactions est les plus dominantes parmi les interactions existantes

Par l'analyse des résultats obtenus en remarque que les ligants étudiés sont réagissent d'une manière différente avec les deux enzymes (NADPH oxydase et la xanthine oxydase), ce qui expliqué la sélectivité des enzymes c'est-à-dire leurs modes d'actions sont basés sur la reconnaissance spécifique du substrat par un domaine particulier chez les enzymes (site actif ou site catalytique). Ainsi l'activité enzymatique est liée à la structure tertiaire de l'enzyme, et notamment à celle du site actif.

De plus la molécule de l'astaxanthine (super antioxydant, le plus puissant des caroténoïdes dans le combat des radicaux libres) a révélé une grande affinité (donc une bonne stabilté et une grande force inhibitrice) *vis-à-vis* les deux catalyseurs enzymatiques par rapport à la zéaxanthine, cette réactivité est due principalement à la variation de la structure.

Donc cette étude apporte des informations sur les mécanismes moléculaires impliqués dans l'activité réductrice de la xanthine oxydase et de la NADPH oxydase *vis-à- vis* de la zéaxanthine et de l'astaxanthine. Elle montre l'importance de la structure moléculaire de ce caroténoïde pour son action biologique et son potentiel thérapeutique.

4. Conclusion

Ce travail qui est axé sur la modélisation moléculaire par docking, a pour but essentiel d'étudier des interactions de nouveaux inhibiteurs sur le NADPH oxydase et la xanthine oxydase, cibles enzymatiques impliquées dans les phénomènes de la production endogène des radicaux libres (facteurs potentialisant l'apparition de très nombreuses maladies tels le diabète, la maladie d'alzheimer, les rhumatismes et les maladies cardiovasculaires…..etc).

Pour mieux comprendre ce phénomène, nous avons focalisé notre discussion sur deux paramètres :

- L'énergie score formée par le complexe Enzyme-Substrat.
- Les interactions moléculaires (non-covalentes) existantes entre ces deux enzymes étudies et les inhibiteurs (astaxanthine et zéaxanthine).

Ces deux paramètres sont utilisés pour expliquer la formation des complexes (Enzyme-Substrat). L'étude de docking moléculaire a révélé que les deux ligands ont des propriétés inhibitrices, ceci justifier par la présence des différents types d'interactions et en plus le ligand de l'astaxanthine possède la plus basse énergie de score par rapport à la zéaxanthine.

5. Références

[1] W. F. van Gunsteren , H. J. Berendsen. Computer Simulation of Molecular Dynamics: Methodology, Applications, and Perspectives in Chemistry. Anger, Chem. lnr. Ed. Engl. 29: 992-1023.1990.
[2] A. R. Leach, Molecular Modelling: Principles and Applications, Longman, 1996.
[3] A. R. Leach Molecular Modelling: Principles and Applications Prentice Hall (Pearson Education), Harlow. 2001.
[5] H. Toulhoat. Modélisation moléculaire. Bases théoriques : des propriétés microscopiques aux propriétés macroscopiques. Techniques de l'ingénieur J 1-13. 2007.
[6] G. Warren, C.W. Andrews, A.M. Capelli, B. Clarke et al. A critical assessment of docking programs and scoring functions, *J. Med. Chem*, 49: 5912-5931, 2006.
[7] S. Smith. The animal fatty acid synthase: one gene, one polypeptide, seven enzymes. *The FASEB Journal*, 8: 1248-1259. 1994.
[8] K.E. Jaeger, T. Eggert. Enantioselective biocatalysis optimized by directed evolution. *Current Opinion in Biotechnology*, 15: 305-313. 2004.

- **Aims and scope:** The Journal of Physical and Chemical Research is an English, French or arabic language peer–reviewed half yearly publication, open access journal, free of charges. The journal edited by: Laboratory of Materials Physics, Radiation and Nanostructures *(*LPMRN), Faculty of Sciences and Technology, Mohamed El Bachir El Ibrahimi University, Bordj-Bou-Arreridj, Algeria. It publishes regular research papers (articles) and short communications. The motivation for this journal is to encourage scientists to publish their experimental and theoretical results in the field of Physical, Chemical and the related subjects. Papers previously published elsewhere cannot be accepted for the journal. Submission must be done at the following email address: jpcr@univ-bba.dz . The acceptance for publication lies on the recommendations of at least two ad hoc referees, and of the editorial board, if necessary.

- **Topics:**
  - Astrophysics and astroparticles
  - Atomic and molecular physics
  - Biological physics
  - Chemical physics and physical chemistry
  - Computational science
  - Condensed matter
  - Fluids and fluid dynamics
  - Gravitation and cosmology
  - Instrumentation and measurement
  - Mathematical physics
  - Medical physics
  - Nuclear physics
  - Optics, quantum optics and lasers
  - Particle physics and field theory
  - Semiconductors
  - Soft matter, liquids and polymers
  - Statistical physics and nonlinear systems
  - Surfaces, interfaces and thin films
  - Thermodynamics
  - Statistical Mechanics and Thermodynamics
  - Molecular Spectroscopy
  - Quantum Chemistry
  - Computational Chemistry
  - Physical Chemistry of Life Sciences
  - Surface Chemistry
  - Catalysis
  - Physical Chemistry of Electrochemistry
  - Kinetics
  - Nanochemistry and Nanophysics
  - Liquid Crystals
  - Ionic Liquid
  - Photochemistry
  - Experimental article of Physical chemistry
  - Mathematical Chemistry

First Legal Deposit: June, 2025